On the drivers of droplet variability in Alpine mixed-phase clouds

Paraskevi Georgakaki[1], Aikaterini Bougiatioti[2], Jörg Wieder[3], Claudia Mignani[4], Fabiola Ramelli[3], Zamin A. Kanji[3], Jan Henneberger[3], Maxime Hervo[5], Alexis Berne[6], Ulrike Lohmann[3] and Athanasios Nenes[1,7]

[1]Laboratory of Atmospheric Processes and their Impacts, School of Architecture, Civil & Environmental Engineering, École Polytechnique Fédérale de Lausanne, Lausanne, CH-1015, Switzerland
[2]Institute for Environmental Research & Sustainable Development, National Observatory of Athens, P. Penteli, GR-15236, Greece
[3]Department of Environmental Systems Science, Institute for Atmospheric and Climate Science, ETH Zurich, Zurich, CH-8092, Switzerland
[4]Department of Environmental Sciences, University of Basel, Basel, CH-4056, Switzerland
[5]Federal Office of Meteorology and Climatology, MeteoSwiss, Payerne, CH-1530, Switzerland
[6]Environmental Remote Sensing Laboratory, School of Architecture, Civil & Environmental Engineering, École Polytechnique Fédérale de Lausanne, Lausanne, CH-1015, Switzerland
[7]Center for Studies of Air Quality and Climate Change, Institute of Chemical Engineering Sciences, Foundation for Research and Technology Hellas, Patras, GR-26504, Greece

Correspondence to: Athanasios Nenes (athanasios.nenes@epfl.ch).

Abstract

Droplet formation provides a direct microphysical link between aerosols and clouds (liquid or mixed phase), and its adequate description poses a major challenge for any atmospheric model. Observations are critical for evaluating and constraining the process. Towards this, aerosol size distributions, cloud condensation nuclei, hygroscopicity and lidar-derived vertical velocities were observed in Alpine mixed-phase clouds during the Role of Aerosols and Clouds Enhanced by Topography on Snow (RACLETS) field campaign in the Davos, Switzerland region during February and March 2019. Data from the mountain-top site of Weissfluhjoch (WFJ) and the valley site of Davos Wolfgang are studied. These observations are coupled with a state-of-the art droplet activation parameterization to investigate the aerosol-cloud droplet link in mixed-phase clouds. The mean CCN-derived hygroscopicity parameter, κ, at WFJ ranges between 0.2-0.3, consistent with expectations for continental aerosol. κ tends to decrease with size, possibly from an enrichment in organic material associated with the vertical transport of fresh ultrafine particle emissions (likely from biomass burning) from the valley floor in Davos. The parameterization provides droplet number that agrees with observations to within ~25%. We also find that the susceptibility of droplet formation to aerosol concentration and vertical velocity variations can be appropriately described as a function of the standard deviation of the distribution of updraft velocities, σ_w, as the droplet number never exceeds a characteristic limit, termed "limiting droplet number", of ~150-550 cm^{-3}, which depends solely on σ_w. We also show that high aerosol levels in the valley, most likely from anthropogenic activities, increase

cloud droplet number, reduce cloud supersaturation (<0.1%) and shift the clouds to a state that is less susceptible to aerosol and become very sensitive to vertical velocity variations. The transition from aerosol to velocity-limited regime depends on the ratio of cloud droplet number to the limiting droplet number, as droplet formation becomes velocity-limited when this ratio exceeds 0.65. Under such conditions, droplet size tends to be minimal, reducing the likelihood that large drops are present that would otherwise promote glaciation through rime splintering and droplet shattering. Identifying regimes where droplet number variability is dominated by dynamical – rather than aerosol – changes is key for interpreting and constraining when and which types of aerosol effects on clouds are active.

1. Introduction

Orographic clouds, and the precipitation they generate, play a major role in Alpine weather and climate (e.g., Roe, 2005; Grubisic and Billings, 2008; Saleeby et al., 2013; Vosper et al., 2013; Lloyd et al., 2015). The formation and evolution of orographic clouds involves a rich set of interactions at different spatial and temporal scales encompassing fluid dynamics, cloud microphysics and orography (Roe, 2005; Rotunno and Houze, 2007). Atmospheric aerosol particles modulate the microphysical characteristics of orographic clouds by serving as cloud condensation nuclei (CCN) that form droplets, or ice nucleating particles (INPs) that form ice crystals (e.g., Pruppacher and Klett, 1997; Muhlbauer and Lohmann, 2009; Zubler et al., 2011; Saleeby et al., 2013).

Emissions of aerosol particles acting as CCN and INPs can affect the microphysical and radiative properties of clouds with strong (but highly uncertain) effects on local and regional climate (IPCC, 2013; Seinfeld et al., 2016). Aerosol interactions with orographic clouds are subject to even larger uncertainties, owing in part to the complex flows generated by the interaction of the large-scale flow with the mesoscale orographic lifting and condensation, and complex anisotropic turbulent air motions that arise (Roe, 2005; Smith, 2006; Rotunno and Houze, 2007). Most importantly, orographic clouds are often mixed-phase clouds (MPCs), which are characterized by the simultaneous presence of supercooled liquid water droplets and ice crystals (Lloyd et al., 2015; Farrington et al., 2016; Lohmann et al., 2016; Henneberg et al., 2017). MPCs remain one of the least understood cloud types, due to the multiple and highly nonlinear cloud microphysical pathways that can affect their properties and evolution. MPCs tend to glaciate (i.e., transition to pure ice clouds) over time because of the Bergeron-Findeisen process, which is the rapid growth of ice crystals at the expense of the evaporating cloud

droplets, owing to the higher saturation vapor pressure of liquid water over ice (Bergeron, 1935; Findeisen, 1938). Aerosol concentrations may also alter the microphysical pathways active in MPCs and ultimately drive their glaciation state. For instance, increase in CCN concentrations leads to more numerous and smaller cloud droplets, reducing the riming efficiency of ice crystals and therefore the hydrometeor crystal mass and the amount of precipitation (Lohmann and Feichter, 2005; Lance et al., 2011; Lohmann, 2017). This mechanism counters the glaciation indirect effect, where increases in INP concentrations elevate ice crystal number concentration (ICNC) and promotes the conversion of liquid water to ice - therefore the amount of ice-phase precipitation (Lohmann, 2002). Increases in CCN can also decrease cloud droplet radius, and impede cloud glaciation, owing to reductions in secondary ice production (SIP), which includes rime splintering, collisional break-up and droplet shattering (Field et al., 2017; Sotiropoulou et al., 2020, 2021).

Cloud-scale updraft velocity (i.e., the part of the vertical velocity spectrum with positive values) is the major driver of droplet formation, owing to the supersaturation generated from adiabatic expansion and cooling (e.g., Nenes et al., 2001; Ghan et al., 2011). Despite its importance, the simulation of updraft velocity by atmospheric models is rarely constrained by observations, which can lead to large uncertainties in climate and numerical weather prediction models (Sullivan et al., 2016, 2018). Reutter et al. (2009) pointed out that droplet formation in clouds can be limited by the amount of CCN present (called the "aerosol-limited" regime), or the vertical velocity that generates supersaturation in the cloudy updrafts (called the "velocity-limited" regime). Over the complex Alpine terrain, vertical motions can be significantly shaped by the effects of orography (Lohmann et al., 2016). Orographic MPCs have been frequently observed in the Swiss Alps under high updraft velocity conditions, where supersaturation with respect to liquid water is formed faster than it is depleted by diffusional and collisional ice growth processes (Korolev and Isaac, 2003) leading to persistent MPCs (Lohmann et al., 2016).

Given the importance of droplet number for the radiative cloud properties and microphysical evolution of Alpine MPCs, it is essential to understand the main aerosol and dynamics properties that drive droplet formation. A limited number of studies exist that discuss this very important topic, focusing though on liquid-phase clouds (Hammer et al., 2014, 2015; Hoyle et al., 2016). Hoyle et al. (2016) showed that 79% of the variance in droplet number in warm clouds formed at the high-altitude Swiss Alps Jungfraujoch station (3450 m a.s.l.) is driven by variations in potential CCN concentration (i.e. aerosol particles with a dry diameter >80 nm). With box model simulations, Hammer et al. (2015) investigated the influence of updraft velocity, particle concentration and hygroscopicity on droplet formation, and found

that variations in vertical wind velocity have the strongest influence on the aerosol activation. The ability to predict droplet number in MPCs, where the existence of ice crystals can deplete supersaturation or the low temperatures may decrease CCN activity through the formation of glassy aerosol, has not been assessed in a closure study to date.

Here we analyze observational data collected as part of the Role of Aerosols and Clouds Enhanced by Topography on Snow (RACLETS) field campaign, which was held in the region of Davos, Switzerland, during February and March 2019. This intensive field campaign aims to address questions related to the modulators of orographic precipitation, the drivers of the enhanced ice-crystal number concentrations observed in MPCs as well as the human-caused pollution effects on cloud microphysical and optical properties. Through this study we focus on a two-week period seeking to unravel the complex aerosol-droplet-updraft velocity interactions that occur in the orographic MPCs. For this, we combine CCN number concentrations with the particle size distributions to understand the variations in hygroscopicity over time and for sites located in the valley and a close by mountain-top site. The in-situ measurements are subsequently coupled with a state-of-the art droplet parameterization to determine the potential droplet numbers and the corresponding maximum supersaturation achieved in cloudy updrafts. The predicted droplet numbers are evaluated against direct observations, and the degree to which droplet formation is velocity- or aerosol-limited is determined for the whole timeseries.

2. Methods

2.1 Observational datasets

The analysis utilizes measurements collected during the RACLETS campaign, which took place from 8 February to 28 March 2019 (https://www.envidat.ch/group/about/raclets-field-campaign) (Mignani et al., 2020; Ramelli et al., 2020b, c; Lauber et al., 2020). This joint research project offers a unique dataset of orographic clouds, precipitation and snow measurements in an effort to shed light on some fundamental microphysical processes being present in subsequent stages of the lifecycle of clouds (i.e. cloud formation, precipitation onset, cloud dissipation). All measurements presented in this paper were performed at two distinct observation stations near Davos, Switzerland (supplement Fig. S1). A measurement site is located at Davos Wolfgang, which is the pass between Davos (1560 m a.s.l.) in the South and Klosters (1200 m a.s.l.) in the North and is otherwise known as Wolfgang-Pass (WOP; 1630 m a.s.l., 46°50’08.076″N 9°51′12.939″E). Measurements were also conducted at the mountain-

top station Weissfluhjoch (WFJ; 2700 m a.s.l., 46°49'58.670″N 9°48′23.309″E), which is located ∽1 km above the valley floor in Davos, in the eastern part of the Swiss Alps. The current study primarily focuses on data collected during a two-week period of interest, which spans from 24 February to 8 March 2019. During the RACLETS campaign, a defective sheath air filter affected the CCN measurements collected at WFJ, thus inhibiting data usage from the instrument for a large duration of the campaign. Therefore, we limit our analysis to the above-mentioned period, when the CCN counter was fully operational. Besides, during the selected period two distinct weather patterns were observed (fair weather conditions interrupted by a precipitating period), allowing for a contrasting analysis of the observed scenarios. The following description refers to the measurements that provided the basis for the present analysis (see Table 1).

2.1.1 Aerosol particle size distribution measurements

Particle size distributions were continuously monitored at WOP and WFJ using commercially available Scanning Mobility Particle Sizers (SMPS; Model 3938, TSI Inc., US). At both stations, the systems consisted of a differential mobility analyzer (Model 3081, TSI Inc., US), a soft X-ray neutralizer (Model 3088, TSI Inc., US) and a water-based condensation particle counter (Model 3787 at WOP, Model 3788 at WFJ, TSI Inc. US). Running the particle counters in low flow mode (0.6 $Lmin^{-1}$), using a sheath flow of 5.4 $Lmin^{-1}$ and applying a total scanning time of 2 minutes (scan time: 97 s, retrace time: 3 s, purge time: 10 s), particle size distributions between 11.5 nm and 469.8 nm diameter were monitored.

2.1.2 CCN measurements

A Droplet Measurement Technologies (DMT) single-column continuous-flow streamwise thermal gradient chamber (CFSTGC; Roberts and Nenes, 2005) was used to carry out in-situ measurements of CCN number concentrations for different supersaturations (*SS*). The CFSTGC consists of a cylindrical flow tube with wetted walls, inside which *SS* is developed by applying a linear streamwise temperature gradient between the column top and bottom. Owing to the greater mass diffusivity of water vapor than the thermal diffusivity of air, a constant and controlled *SS* is generated with a maximum at the centerline of the flow tube. The *SS* is mainly dependent on the applied temperature gradient, flow rate and pressure (Roberts and Nenes, 2005). An aerosol sample flow is introduced at the column centerline, and those particles having a critical supersaturation lower than the instrument *SS* will activate to form droplets and will afterward be counted and sized by an Optical Particle Counter (OPC) located

at the base of the CFSTGC column. The *SS* developed within the instrument responds linearly to changes in pressure, since its operation relies on the difference between heat and mass diffusivity. Calibration of the instrument, which determines the output supersaturation, was performed by the manufacturer at ~800 mbar, while throughout the campaign the CFSTGC was operating at a lower pressure ~735 mbar, therefore the *SS* reported by the instrument is adjusted by a factor of $\frac{735}{800} = 0.92$, which accounts for the difference between the ambient and the calibration pressure (Roberts and Nenes, 2005). CCN concentrations were measured at a specific *SS* for approximately 10 minutes; the instrument was cycled between 6 discrete values ranging from 0.09% to 0.74% supersaturations, producing a full spectrum every hour. Each 10-minute segment of the raw CCN data are filtered to discount periods of transient operation (during supersaturation changes), and whenever the room temperature housing the instrument changed sufficiently to induce a reset in column temperature (the instrument control software always sets the column temperature to be at least 1.5 degrees above the room temperature to exclude spurious supersaturation generation in the column inlet). The CFSTGC was deployed on the mountain-top site of WFJ with the intention of relating the CCN measurements directly to the size distribution and total aerosol concentration data measured by the SMPS instrument at the same station.

2.1.3 Cloud microphysical measurements

In-situ observations of the cloud microphysical properties were obtained with the tethered balloon system HoloBalloon (Ramelli et al., 2020a). The main component of the measurement platform is the holographic cloud imager HOLIMO 3B, which uses digital in-line holography to image an ensemble of cloud particles in the size range from 6 μm to 2 mm diameter in a three-dimensional detection volume. Note that particles smaller than 6 μm are not detected by HOLIMO, which means that the droplet number concentration may be underestimated. Based on a set of two-dimensional images, information about the particle position, size and shape can be obtained. The detected particles can be classified as cloud droplets and ice crystals using supervised machine learning (Fugal et al., 2009; Touloupas et al., 2020). The differentiation between cloud droplets (circular) and ice crystals (non-circular) is done for particles exceeding 25 μm diameter based on their shape (Henneberger et al., 2013). From the classification, the phase-resolved size distribution, concentration and content can be derived (Henneberger et al., 2013; Ramelli et al., 2020a). The HoloBalloon platform was flying at WOP and provided vertical profiles of the cloud properties within the lowest 300 meters of the boundary layer

(BL). The current analysis utilizes the cloud droplet number concentration and liquid water content (LWC) measurements. Note that the LWC is calculated based on the size distribution of the cloud droplets using a liquid water density (ρ_w) of 1000 kg m^{-3} and is therefore dominated by large cloud particles.

Table 1. Overview of data sources from the RACLETS campaign used for this study. Along with the observed parameters, the corresponding instrumentation, measurements range and time resolutions are listed.

Measured parameter	Measurement site	Instrument	Measurement range	Time resolution
Aerosol number size distribution	WOP/ WFJ	Scanning Mobility Particle Sizer	11.5 – 469.8 nm	2 min
CCN number concentration	WFJ	Continuous flow streamwise thermal gradient CCN counter	*SS* = 0.09 – 0.74%	1 s
Cloud droplet number concentration and liquid water content	WOP	Holographic cloud imager HOLIMO	6 μm – 2 mm	10 – 20 s
Precipitation	WOP/ WFJ	Parsivel disdrometer/ MeteoSwiss weather station	0.2 mm – 25 mm	30 s
Horizontal wind speed and direction	WOP/ WFJ	MeteoSwiss weather station	–	10-min averages
Profiles of vertical wind speed	WOP	Wind Doppler Lidar	200 m – 8100 m AGL	5 s max

2.1.4 Meteorological data

During the measurement period, meteorological parameters (e.g., pressure, temperature, precipitation, horizontal wind speed and direction) were continuously monitored by the permanent MeteoSwiss observation station at WFJ. Additionally, a weather station was installed on the OceaNet container (Griesche et al., 2019) deployed at WOP, which also hosted

several remote sensing instruments (e.g., Cloud radar, Raman Lidar, Microwave radiometer) and a Particle Size Velocity (Parsivel) disdrometer (Parsivel2, OTT HydroMet GmbH, Germany; Tokay et al., 2014) to measure precipitation. As there was no wind sensor included in the weather station on the OceaNet container, we utilized the horizontal wind speed and direction measurements from the nearby MeteoSwiss station in Davos, assuming that they provide a good proxy for the wind regime in the valley. Vertical wind speed profiles were obtained with a wind Doppler Lidar (WindCube 100S, manufactured by Leosphere) at WOP. Throughout the campaign the wind lidar measured from 200 m to 8100 m above ground level (AGL) with high temporal (5 s max) and vertical resolution (50 m). The wind lidar operated following the Doppler Beam Switching technique with an elevation of 75˚. More information about the remote sensing measurements can be found in Ramelli et al. (2020b).

2.2 Aerosol hygroscopicity

The aerosol hygroscopicity parameter, κ, encompasses the impact of particle chemical composition on its subsaturated water uptake and CCN activity (Petters and Kreidenweis, 2007). Here, we determine κ similar to the approach of Moore et al. (2011), Jurányi et al. (2011), Lathem et al. (2013), Kalkavouras et al. (2019), Kacarab et al. (2020) and others, by combining the CCN measurements with the SMPS aerosol size distribution data as follows. For each SMPS scan, the particle size distribution is integrated backward starting from the bin with the largest-size particles – which corresponds to CCN with the lowest critical supersaturation, S_{cr}. We then successively add bins with smaller and smaller diameters, until the aerosol number matches the CCN concentration observed for the same time period as the SMPS scan. The particles in the smallest size bin, which we call *critical dry diameter*, D_{cr}, correspond to CCN with highest S_{cr} possible – being the instrument supersaturation, *SS*. From D_{cr} and *SS* we determine κ from Köhler theory (Petters and Kreidenweis, 2007), assuming the particle chemical composition is internally mixed:

$$\kappa = \frac{4A^3}{27 D_{cr}^3 SS^2} \quad (1)$$

where $A = \frac{4M_w\sigma}{RT\rho_w}$ is the Kelvin parameter, while M_w (kg mol^{-1}) is the molar mass of water, σ (J m^{-2}) is the surface tension of the solution droplet, R is the universal gas constant and T (K) is the ambient temperature. Here we assume the surface tension of the solution droplet is equal to that of pure water ($\sigma = \sigma_w$) by convention. The κ determined above represents the composition of particles with diameter D_{cr} (large particles can have a different κ but still activate given that

their S_{cr} is lower than the prevailing *SS* in the CCN chamber). This means that over the course of an hour, over which a full *SS* cycle is completed, κ is determined for a range of D_{cr}, which in our case were in the range of 50-200 nm (Section 3.1). This size-resolved κ information provides insights on the possible origin and chemical components of the aerosol, which is important given that there is no other measurement available to constrain chemical composition during RACLETS. From κ, we infer an equivalent organic mass fraction, ε_{org}, assuming that the aerosol is composed of an organic-inorganic mixture:

$$\varepsilon_{org} = \frac{(\kappa - \kappa_i)}{(\kappa_o - \kappa_i)} \quad (2)$$

where κ_i = 0.6 and κ_o = 0.1 are characteristic hygroscopicity values for the inorganic fraction of aerosol (represented by ammonium sulphate), and organic aerosol, respectively (Petters and Kreidenweis, 2007; Wang et al., 2008; Dusek et al., 2010). Note that these values for a continental aerosol are supported by observations and analyses (e.g., Andreae and Rosenfeld, 2008; Rose et al., 2008; Pringle et al., 2010).

2.3 Cloud droplet number and cloud maximum supersaturation

Here we apply adiabatic cloud parcel theory to the observational datasets to determine the maximum in-cloud supersaturation (S_{max}) and cloud droplet number (N_d) that would form over both measurement sites throughout the observation period. Droplet calculations are carried out with the physically based aerosol activation parameterization of Nenes and Seinfeld (2003), with extensions introduced by Fountoukis and Nenes (2005), Barahona et al. (2010), and Morales and Nenes (2014). Each N_d calculation requires knowledge of the observed pressure, temperature, vertical winds, aerosol size distribution and hygroscopicity. For the WFJ site, all data are available as described in the sections above. For the WOP site, CCN (hence hygroscopicity) data are not available, so we carry out N_d calculations at two κ values, 0.1 and 0.25, which is the upper and the lower limit determined from the WFJ analysis (Section 3.1). The ability to reproduce observed cloud droplet number concentrations ("Method evaluation", Section 3.2.1) further supports the selection of these values.

The wind lidar measurements conducted at WOP (Section 2.1.4) are used to determine the prevailing vertical velocities at both sites. Data extracted from the first bin of the lidar, being 200 m AGL, are considered representative for WOP as the wind lidar has no values very close to the ground, while measurements extracted for 1100 m AGL are used as a proxy for the vertical velocities at WFJ. The high resolution wind lidar data are grouped by hour and each

fitted to half-Gaussian probability density functions (PDFs) with zero mean and standard deviation σ_w. An hourly PDF of updraft velocities is provided in the supplementary material as an example of the calculation method we followed here (supplement Fig. S2). Employing the "characteristic velocity" approach of Morales and Nenes (2010), the PDF-averaged values of N_d and S_{max} are calculated by applying the parameterization using a single characteristic velocity, $w^*=0.79\sigma_w$. This approach has been shown to successfully predict cloud-scale values of N_d in field studies for cumulus and stratocumulus clouds (e.g., Conant et al., 2004; Meskhidze et al., 2005; Fountoukis et al., 2007; Kacarab et al., 2020). The droplet closure carried out in this study is also used to support the validity of this approach for Alpine MPCs. To determine the σ_w values used in the closure study (Section 3.2.1), we isolated the segments of the wind lidar measurements that correspond to each cloud event observed by the Holoballoon platform. The subsequent fitting of the measured updraft velocities to half-Gaussian PDFs revealed a σ_w value representative of each cloud. The accuracy of the wind lidar products is affected by precipitation, as the measured updraft velocities might be masked by the terminal fall velocity of the hydrometeors. We therefore exclude precipitating periods from our analysis – using disdrometer measurements to constrain periods of precipitation. Aiming to examine how N_d responds to different vertical velocity-aerosol situations, as a sensitivity test, potential N_d for both sites are calculated at 10 values of σ_w between 0.1 and 1.0 ms^{-1} that cover the observed range (Section 3.2.4). Note that we use the term "potential" droplet number throughout this study, as its calculation is performed regardless of the actual existence of clouds over the measurement sites.

3. Results and discussion

3.1 Particle number, CCN concentration and κ at WOP and WFJ

The total aerosol number concentration (N_{aer}) timeseries (integrated aerosol size distribution) together with horizontal wind speed and direction measurements are depicted for both sites in Figure 1. The N_{aer} data points of WFJ are colored by κ (Section 2.2), while the orange solid line is used as a trace for WOP timeseries, as κ was not determined for the site owing to a lack of corresponding CCN measurements. Aiming to interpret the aerosol variations and the potential differences observed between valley and high-altitude measurements, the two-week period of interest is divided into two different sub-periods. During 24 and 28 of February, a high-pressure system was dominant over Europe with clear skies and elevated temperatures (supplement Fig. S3). During this first sub-period, the N_{aer} varies considerably, and tends to

follow a diurnal cycle that anticorrelates between the two sites (Fig. 1a). The concentrations at WOP are most of the times elevated with respect to WFJ, which is expected as the N_{aer} in the valley is higher – being influenced by local sources, which during this time of the year include emissions from biomass burning (BB) (Lanz et al., 2010). N_{aer} at WOP peaks in the evening, reaching up to $\backsim 10^4$ cm^{-3} presumably because of BB emissions in the valley which seem to stop around midnight (Fig. 1a). Up to 2 orders of magnitude lower N_{aer} is measured at the same time at the WFJ site. In the afternoon, aerosol concentrations at WFJ approach those observed at WOP, indicating that the two sites are possibly experiencing similar air masses. The κ for WFJ seems to follow a clear temporal pattern as well, ranging between $\backsim$0.1-0.4 with a minimum in the afternoon, when the two sites experience the same air masses. Low N_{aer} values are accompanied by higher κ, while at higher N_{aer} conditions less hygroscopic aerosols are recorded (Fig. 1a).

The above diurnal cycles and their relationships can be understood in terms of BL dynamics typically occurring in mountain-valley systems (Chow et al., 2013). During daytime, under clear sky conditions, the slopes and the valley itself are warmed by solar radiation, causing rising of the BL, and additionally the production of buoyant air masses that rise up the slope toward the summit (through "up-slope" and "up-valley" winds) (Okamoto and Tanimoto, 2016). This hypothesis can be further supported by the fair weather recorded by the weather station at WFJ until 28 February (supplement Fig. S3). The buoyant upslope flow could then transport polluted air masses originating from the BL of the valley up to the WFJ site, elevating the concentrations of less hygroscopic aerosols observed in the afternoon. The situation reverses during nighttime, when cold air descends from the slopes (down-slope winds) and flows out of the valley (down-valley winds) due to the radiative cooling of the surface. The less polluted air observed during the early hours of the day before sunrise indicates that the WFJ station remained in the free troposphere (FT), with lower N_{aer} and more aged air (i.e. larger κ) with a more prominent accumulation mode (Baltensperger et al., 1997; pp. 376-378 in Seinfeld and Pandis, 2006; Kammermann et al., 2010; Jurányi et al., 2011).

Another consideration is that the upslope flow that "connects" the valley and the mountain-top site may not only be driven by thermal convection but also from mechanically-forced lifting. The latter mechanism is caused by the deflection of strong winds by a steep mountain slope and it can be of great importance depending mainly on the height of the mountain and the mean speed of the wind (Kleissl et al., 2007). The local wind effects can be further interpreted looking at the MeteoSwiss timeseries of wind speed and direction for both stations (Fig. 1b, c). Wind measurements at WFJ station recorded a strong wind speed reaching

up to ∽11 ms^{-1} from easterly-northeasterly directions between 24 and 28 of February. The wind direction measured at WFJ coincides with the relative location of WOP site (see black dashed line in Fig. 1c). The steep orography over the Alps would transform part of this strong horizontal motion into vertical motion, and transport air from WOP to WFJ, as seen in other Alpine locations, like Jungfraujoch (e.g., Hoyle et al., 2016). A detailed analysis however is out of the scope of this study.

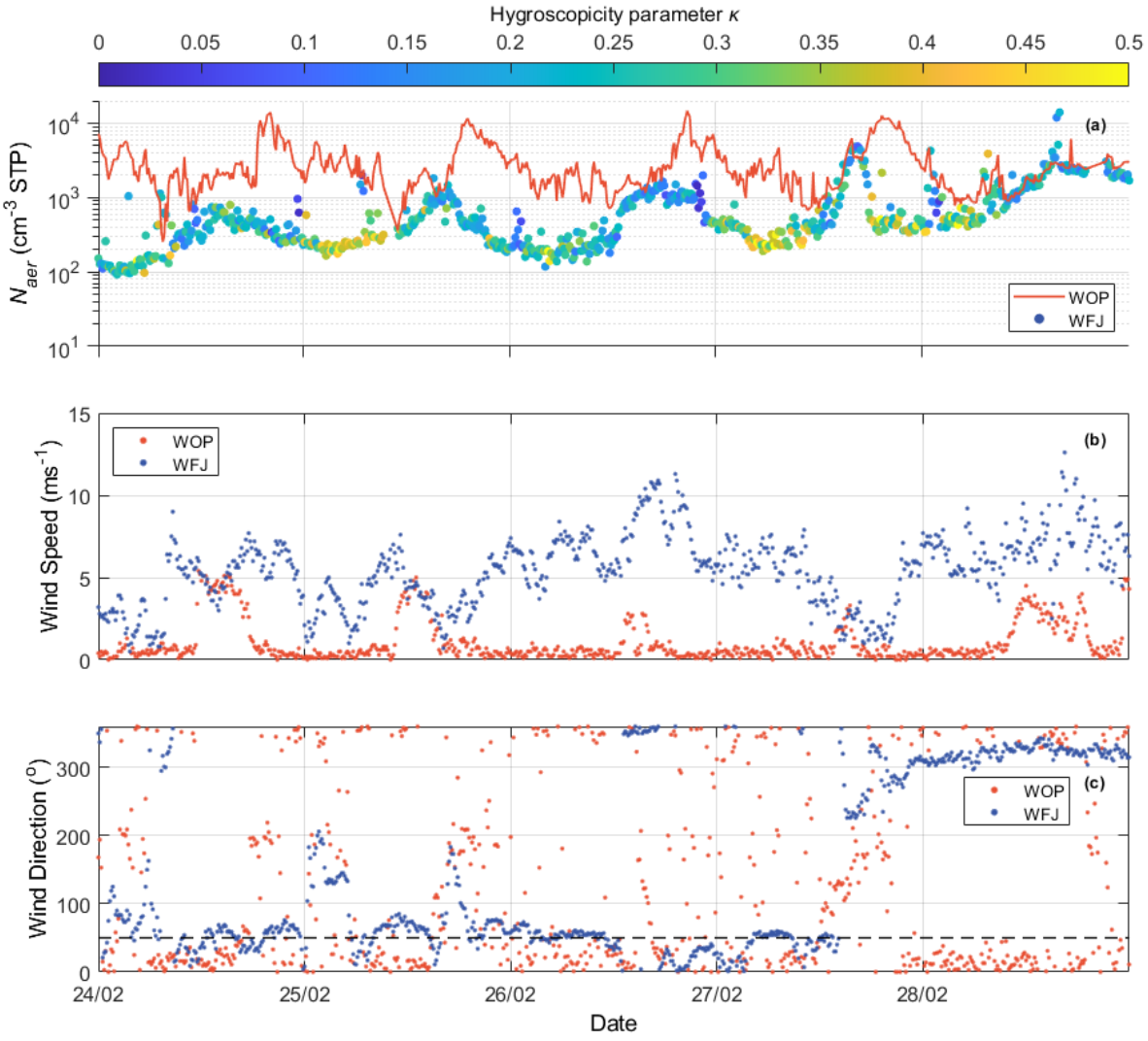

Figure 1. (a) N_{aer} in standard temperature and pressure conditions (cm^{-3} STP) at WOP (orange line) and at WFJ (circles colored by κ), (b) wind speed (ms^{-1}), and (c) wind direction (in degrees) obtained from the MeteoSwiss observation stations at WFJ (blue dots) and Davos (orange dots) between 24 and 28 February 2019. The black dashed line indicates the relative direction of WOP to WFJ. Each day is referenced to 00 UTC.

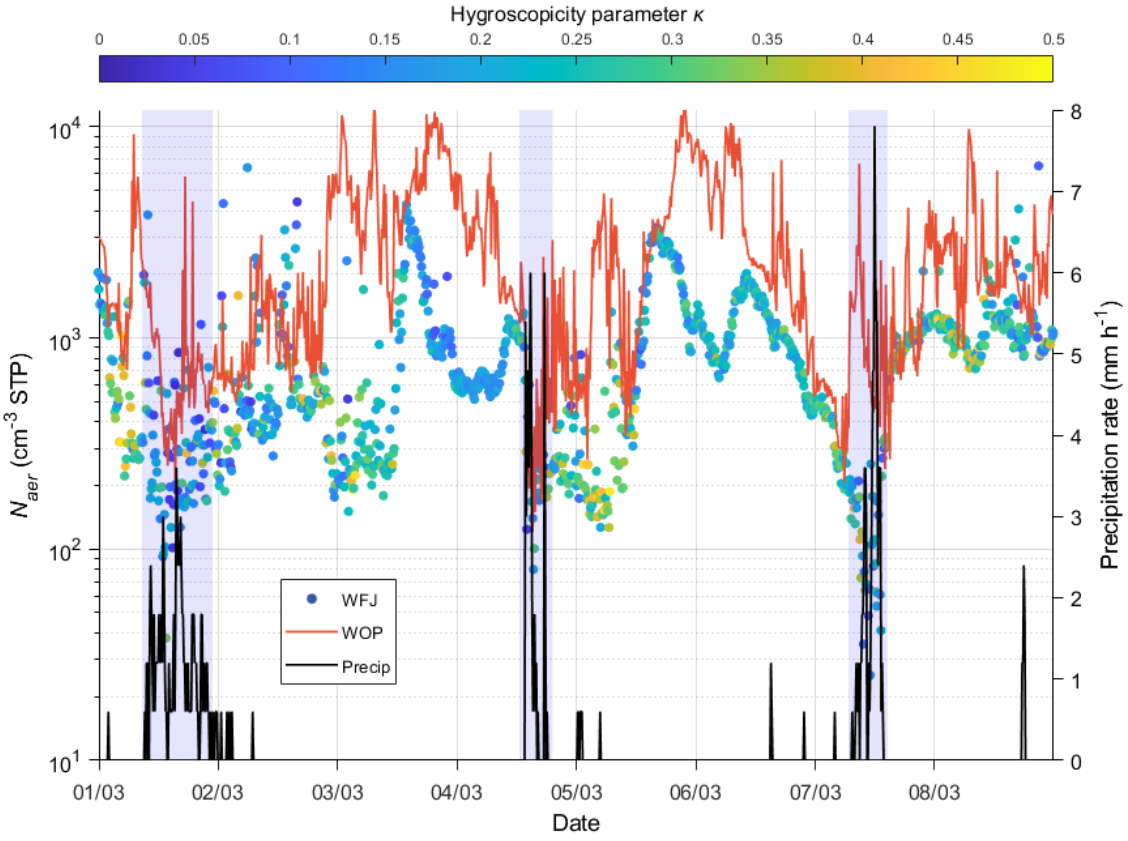

Figure 2. N_{aer} (cm^{-3} STP) at WOP (orange line) and at WFJ (circles colored by κ). The black solid line represents the precipitation rate (mm h^{-1}) recorded from the MeteoSwiss observation station for each 10-min interval at WFJ between 1 and 8 of March 2019. The blue-shaded areas represent the periods when precipitation recoded at WFJ site is most intense.

Similar to Figure 1a, Figure 2 illustrates the N_{aer} timeseries measured at both sites along with the precipitation rate recorded by the MeteoSwiss station at WFJ during the time period between 1 and 8 March 2019. Meteorological observations show the pressure and temperature dropping (supplement Fig. S3) together with intense snow and rain events, associated with the passage of cold fronts over the region. Three intense precipitation events are visible in our dataset occurring on the 1st, 4th and 7th of March 2019 (blue-shaded areas on Fig. 2) creating up to 7.8 mm per hour of precipitation. The most intense drop in N_{aer} is seen to occur during and after the precipitation events, with the aerosol concentrations dropping to less than 200 cm^{-3} (100 cm^{-3}) at WOP (WFJ). This is not the case for the last event, where a big "spike" of N_{aer} is observed before the precipitation event in WOP timeseries, which is in contrast with the concurrent sharp decrease in N_{aer} (< 20 cm^{-3}) observed at WFJ. This could be an indication of a local source affecting the N_{aer} recorded in the valley. During dry weather conditions, we can notice again the aerosol timeseries correlating during the afternoon and anticorrelating later in the evening-early morning hours. On March 3, a steep increase in N_{aer} is seen in WFJ timeseries

reaching up to ∽4000 cm^{-3}, which is followed by a period of several hours with low hygroscopicity values ($\kappa < 0.2$) indicating once more the influence of freshly emitted particles arriving at WFJ from the BL of lower altitudes. Additionally, between 1 and 8 March, the diurnal cycle of particle hygroscopicity is less pronounced compared to the period between 24 and 28 February. Especially on the 1st and 7th of March, less hygroscopic aerosols ($\kappa < 0.1$) - hence less effective CCN particles - are found at WFJ (Fig. 2). This is likely from either precipitation removing aerosol through diffusive and impaction processes, or, the removal of aerosol particles that first activate and then are removed by precipitation. Also, because N_{aer} drops, fresh local emissions become more important, further justifying the predominance of low hygroscopicity values.

Figure 3 presents the CCN number concentration timeseries measured at ambient conditions at WFJ for all 6 supersaturations. Throughout the two-week measurement period the recorded CCN number concentrations do not seem to follow a clear temporal pattern. The absence of a diurnal cycle in CCN properties measured at Jungfraujoch during winter was also pointed out in the study of Jurányi et al. (2011), because the site is mainly in free tropospheric conditions during most of the winter. According to Figure 3, the observed CCN concentrations tend to be low (∽10^2 cm^{-3}) even at the highest *SS* (0.74%), which is expected given that WFJ is a remote continental measurement site with CCN concentrations that are typical of free tropospheric continental air (Jurányi et al., 2010, 2011; Hoyle et al., 2016; Fanourgakis et al., 2019). This is again in line with the measured monthly median values of CCN (at *SS* = 0.71%) reported by Jurányi et al. (2011) being equal to 79.1 and 143.4 cm^{-3} for February and March 2009, respectively. Some local CCN spikes are however recorded during the evening of 28 February and at the beginning of March (e.g., on 2nd, 4th and 6th March), with the observed values of CCN reaching up to 650 cm^{-3} at SS=0.09% (lowest SS) and 1361 cm^{-3} at *SS*=0.74% (highest *SS*). Considering that WFJ is a site frequently located in the FT, sudden fluctuations in the CCN concentrations could be related to the vertical transport of freshly emitted particles (e.g., wood burning or vehicle emissions) from the valley floor in Davos. It is also worthy to note that some aerosol spikes observed on the 3rd (∽ 3350 cm^{-3}) and the 5th of March (∽ 2100 cm^{-3}) in the WFJ timeseries (Fig. 1a) are not accompanied by a corresponding peak in the CCN timeseries. This indicates the presence of small aerosol particles, which activate above 0.74% supersaturation (i.e. particles with a diameter smaller than ∽ 25 nm). This event could also be associated with new particle formation (NFP) events. A previous study by Herrmann et al. (2015) reported the aerosol number size distribution at the Jungfraujoch over a 6-year period

indicating that NPF was observed during 14.5% of the time without a seasonal preference. Tröstl et al. (2016) also showed that NPF significantly adds to the total aerosol concentration at Jungfraujoch and is favored only under perturbed FT conditions (i.e. BL injections). Finally, during the three intense precipitation events (on 1st, 4th and 7th March) we can identify again that the wet removal of the more hygroscopic aerosol (Fig. 2) suppresses the presence of cloud-activating particles, at times depleting the atmosphere almost completely from CCN (Fig. 3). This is clearly shown on the 1st and the 7th of March, when the CCN number measured at 0.74% supersaturation drops below 10 cm^{-3}, which is extremely low for BL concentrations.

The aerosol hygroscopicity parameter derived from all CCN data collected between 24 of February and 8 of March is presented in Figure 4a. The red solid line represents the hourly averaged hygroscopicity values over one complete instrument supersaturation cycle. The hygroscopic properties of the particles at WFJ vary as a function of supersaturation, exhibiting on average lower values (~0.1) at high *SS* and higher values (∽0.3) at the lower *SS*. Since the supersaturation inversely depends on particle size, Figure 4a indicates that the hygroscopicity of the particles drops by almost 60% as the particles are getting smaller (i.e. as the supersaturation increases). Table 2 summarizes the mean values of κ and D_{cr} and their standard deviations, as calculated for each measured *SS*. The anticorrelation seen between the instrument *SS* and D_{cr} is reasonable, if we consider that the latter represents the minimum activation diameter in a population of particles, and therefore only the particles with a D_{cr} >193.54 nm are able to activate into cloud droplets at low *SS* values (0.09%). The hourly averaged hygroscopicity at each *SS* slot falls within a range of ∽0.2 and ~0.3, which is a well representative value of continental aerosols (Andreae and Rosenfeld, 2008; Rose et al., 2008).

Table 2. Average κ and D_{cr} values at WFJ for each *SS* measured between 24 February and 8 March 2019. Uncertainty for each value is expressed by the standard deviation.

SS (%)	κ_{mean}	$D_{cr,mean}$
0.09	0.26 ± 0.10	193.54 ± 29.58
0.18	0.31 ± 0.13	116.80 ± 22.20
0.28	0.25 ± 0.13	96.69 ± 21.62
0.37	0.24 ± 0.13	82.67 ± 20.93
0.55	0.20 ± 0.12	68.30 ± 20.95
0.74	0.19 ± 0.11	58.11 ± 17.54

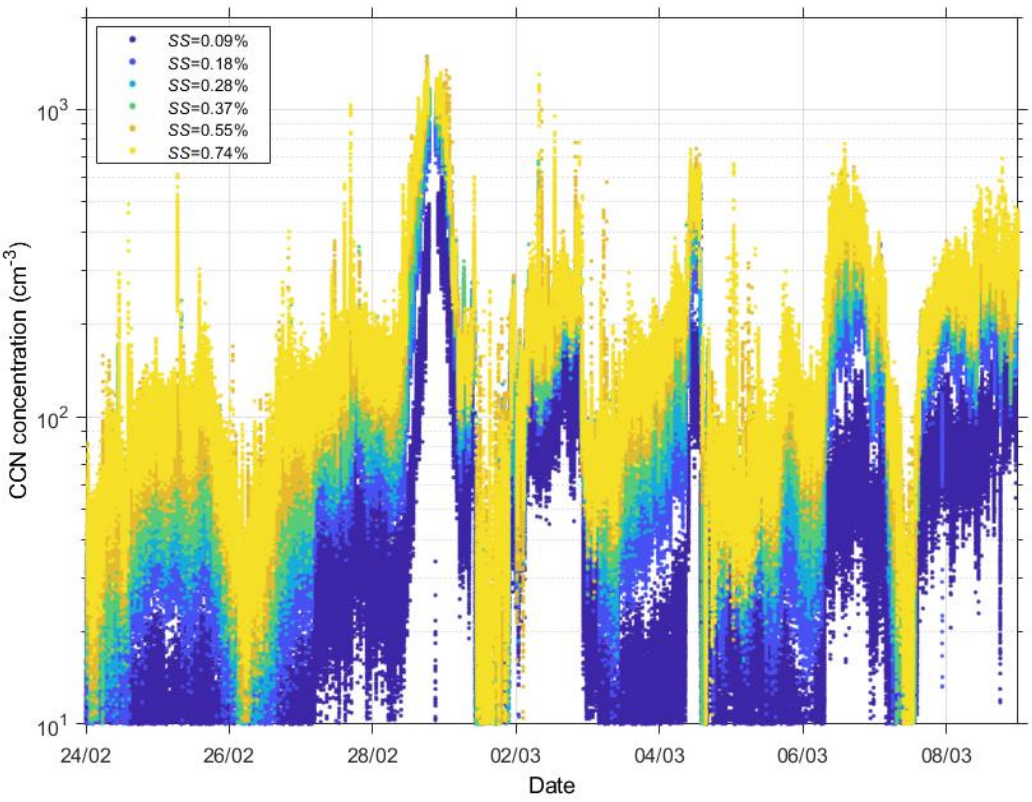

444

445 **Figure 3.** Timeseries of in-situ CCN number concentrations (cm^{-3}) at WFJ for different levels
446 of supersaturation (*SS*) with respect to water between 24 February and 8 March 2019.

447

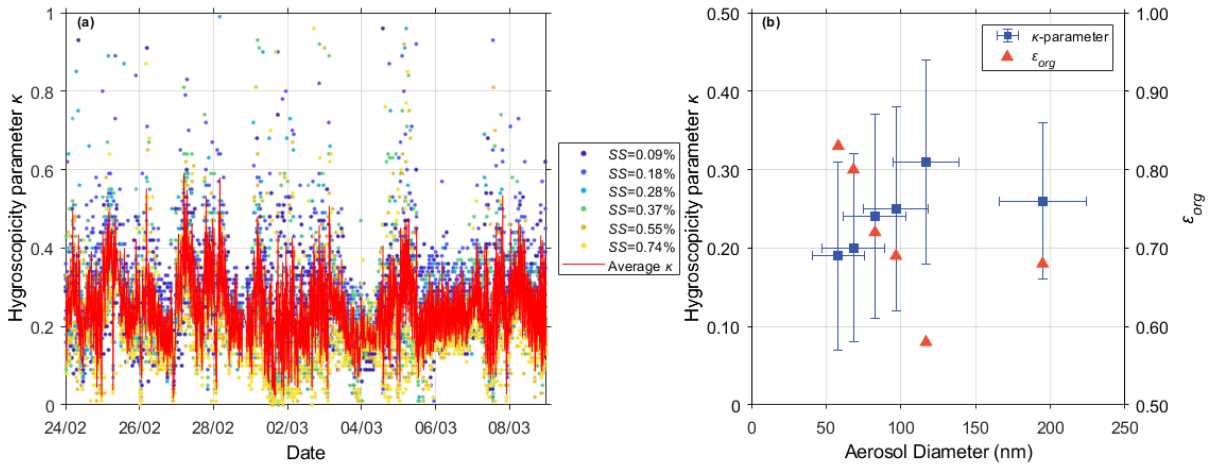

448

449 **Figure 4.** (a) Timeseries of the hygroscopicity parameter κ at WFJ at different levels of
450 instrument supersaturation (0.09–0.74%) throughout the period of interest. The solid red line
451 indicates the hourly averaged κ timeseries over a complete *SS* cycle. (b) Size-resolved aerosol
452 hygroscopicity (blue squares) and the respective ε_{org} (orange triangles) calculated for the WFJ
453 site.

454

The hygroscopicity parameter along with the inferred ε_{org} (Eq. 2) is shown in Figure 4b as a function of particle size. Compared to smaller particles, the higher κ of larger particles (>100 nm) is consistent with them being more aged and with a lower fraction of organics. The smaller particles are possibly enriched in organic species, which is consistent with the notion that airmasses in the valley can contain large amounts of freshly emitted BB smoke with lower κ. Aerosol particles in the FT are considerably more aged (pp. 376-378 in Seinfeld and Pandis, 2006) and exhibit higher values of κ and consequently lower values of ε_{org}. The chemical composition of sub-100 nm particulate matter was therefore presumably dominated by organic material transported from the valley, while the higher κ values characterizing the larger particles are consistent with the more aged character of free tropospheric aerosols (e.g., Jurányi et al., 2011). The higher ε_{org} inferred for the smaller particles suggests that mixing between fresh emissions in the valley and the free tropospheric aerosol might also be taking place at WFJ.

3.2 Potential cloud droplet number concentration and maximum supersaturation

3.2.1 Method evaluation

During the RACLETS campaign, planar and dendritic ice particles were collected from supercooled clouds at WFJ aiming to examine their refreezing ability. A detailed description of the sampling methodology can be found in Mignani et al. (2019). Between March 1 and March 7, images of single dendrites were taken and analyzed visually for the degree of riming (supplement Fig. S4). The estimated riming degree varies from 1 (lightly-rimed) to 4 (heavily-rimed) following the categorization of Mosimann et al. (1994). Some representative images of each measured riming degree are shown in Figure S4b. Although images were captured intermittently, they were taken within all three intense precipitating events occurring during the period of interest (blue-shaded areas on Fig. 2). All dendrites captured were at least lightly rimed (i.e. riming degree = 1), which provides direct evidence for the co-existence of supercooled droplets and ice in clouds. Except the indirect evidence of the presence of MPCs over WFJ, Figure 5 provides an overview of the direct microphysical measurements carried out by the Holoballoon at WOP (Section 2.1.3). Three cloud events are sampled during the 7th and the 8th of March, a more detailed description of which can be found in Ramelli et al. (2020b, c). The observed low-level clouds are likely produced by orographic lifting when the low-level flow is forced to ascent over the local topography from Klosters to WOP producing local updrafts and thus water supersaturated conditions. The cloud LWC measurements from the

holographic imager display significant temporal variability that is also related to variations in the altitude of the tethered balloon system, as it tends to follow an adiabatic profile (Fig. 5a, b). Deviations from the adiabatic LWC profile are likely caused by entrainment of dry air within the low-level clouds. Departures during the mixed-phase conditions recorded on March 8 (Fig. 5b), could also be attributed to the depletion of N_d through riming and depositional growth. These two processes are frequently found to enhance orographic precipitation in feeder clouds. Indeed, a large fraction of rimed ice particles and graupel were observed that day with HOLIMO between 17:00 and 17:40 UTC (Ramelli et al., 2020c). Throughout the two-day dataset presented in Figure 5, the HoloBalloon system samples at altitudes lower than 300 m AGL, providing observations that are representative of BL conditions.

The observed N_d timeseries collected at WOP are illustrated in Figures 5c and 5d. The measurements corresponding to LWC < 0.05 gm^{-3} are filtered out from the analysis, assuming that they do not effectively capture in-cloud conditions. A similar criterion for LWC was also applied in Lloyd et al. (2015) to determine the periods when clouds were present over the Alpine station of Jungfraujoch. Since the measured cloud properties have finer resolution (10-20 secs) than the predicted ones, the observed dataset is averaged every 2 minutes. On March 7, the balloon-borne measurements were taken in a post-frontal air mass (i.e. passage of a cold front in the morning) and indicated the formation of two low-level liquid layers (Fig. 5c) over WOP, which is attributed to low-level flow blocking (Ramelli et al., 2020b). Note that small droplets (< 6 μm) cannot be detected by HOLIMO (Section 2.3.1) and therefore the reported N_d should be considered as a lower estimate. The influence of small cloud droplets, however, on the reported LWC is minor, since the contribution of the larger cloud droplets dominates. During the first cloud event, an N_d of up to ∽100 cm^{-3} was recorded, while slightly increased N_d in the range of ∽50-120 cm^{-3} is visible during the second cloud event. On March 8, a small-scale disturbance passed the measurement location Davos, which brought precipitation (Ramelli et al., 2020c). During the passage of the cloud system, the in-situ measurements collected at WOP revealed the presence of a persistent low-level feeder cloud confined to the lowest 300 m of the cloud. The mixed-phase low-level cloud that is shown in Figure 5d, turned into an ice-dominated low-level cloud after 18 UTC (not shown). Throughout this event, N_d seems to range between ∽100-350 cm^{-3} (Fig. 5d), while the observed ICNC was in the range of ∽1-4 L^{-1} (see Fig. 6b in Ramelli et al., 2020c).

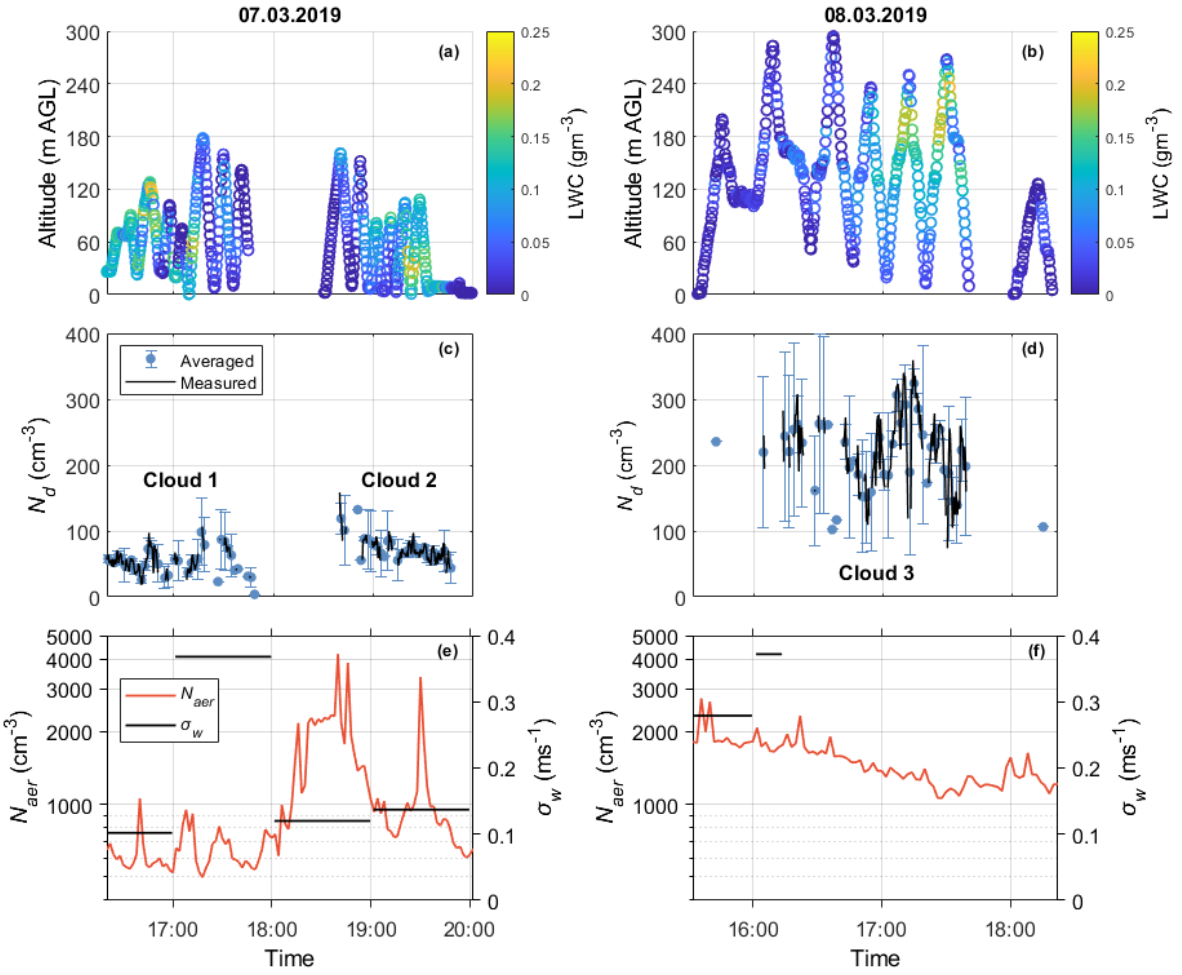

Figure 5. Timeseries of the 7th (left panels) and the 8th (right panels) of March, showing the vertical profiles of the LWC (gm^{-3}) in (a) and (b), the filtered (black lines) and the 2-minute averaged (cyan circles) N_d (cm^{-3}) measured at WOP with the HoloBalloon platform in (c) and (d), and the corresponding SMPS aerosol concentrations (cm^{-3}) (orange line) and the hourly wind-lidar derived σ_w values (ms^{-1}) (black line) in (e) and (f). Error bars represent the standard deviation of N_d during the averaging period.

According to Figures 5e and 5f, low N_{aer} (<10^3 cm^{-3}) and intermediate σ_w values are representative of the period throughout which the first cloud formed, while up to 4 times higher N_{aer} is observed during the following two cloud events, with relatively low σ_w values characterizing the second cloud compared to the third one. On March 8, the disdrometer recorded rainfall over WOP, starting a few minutes after the development of the observed cloud system, reflected in the removal of updraft velocity measurements after 16:15 (Fig. 5f). Note that the concentration measurements presented in Figure 5 correspond to ambient temperature and pressure conditions. The contrasted aerosol and vertical velocity regimes, in which the observed clouds are formed, offer a great opportunity to test how the proposed methodology performs under a wide range of aerosol and velocity conditions. Indeed, the mean cloud droplet

diameters exhibit a wide range of values, which for WOP range between 10 μm and 17 μm on March 7, and 8 μm to 12 μm on March 8 (not shown).

The N_d closure performed for the three cloud events observed over WOP during the last two days of the period of interest is presented in Figure 6. Note that the potential droplet formation is evaluated using the updraft velocity PDF calculated for each cloud period, rather than the hourly σ_w data shown in Figures 5e and 5f (Section 2.3). Owing to the precipitation occurrence during March 8, we focused on the 15-min time period between 16:00 and 16:15 to determine a relevant updraft velocity from the wind lidar measurements representative of Cloud 3. The Gaussian fit to the updraft velocities gave a distribution with σ_w = 0.24 and 0.16 ms^{-1} for the first two clouds present on the 7th of March, and, σ_w = 0.37 ms^{-1} for the cloud system observed on the 8th of March. The w^* values used to apply the droplet parameterization are therefore between 0.1-0.4 ms^{-1} (Section 2.3). Figure 6 indicates that the parameterization predictions agree to within 25% with the in-situ cloud droplet number concentrations. A similar degree of closure is frequently obtained for other in-situ studies (e.g., Meskhidze et al., 2005; Fountoukis et al., 2007; Morales et al., 2011; Kacarab et al., 2020), which however focused on liquid-phase clouds. Here we show that the methodology can also work for MPCs (i.e. Cloud 3 in Fig. 6). It is important to note here that part of the discrepancy between prediction and measurement could also be related to the underestimation of the measured N_d (Section 2.1.3). Hence, an even better degree of closure is likely. The good agreement between measurements and predictions - even under mixed-phase conditions, reveals that processes like condensation freezing and the removal of cloud droplets through riming and collision-coalescence are not disturbing the S_{max} and hence the N_d predicted by the parameterization, at least for the given clouds. Pre-existing liquid and ice hydrometeors falling to the examined cloud levels might also deplete the supersaturation affecting the number of the activated droplets. The contribution of supersaturation depletion can readily be included in the droplet activation parameterization (Sud et al., 2013; Barahona et al., 2014) but is not considered in this study. Furthermore, the parameterization predictions indicate that the best fit is achieved using a κ of $\backsim$0.1 (Fig. 6). N_{aer} at WOP is likely dominated by lower κ values, indicating that the particles are getting richer in organic material, compared to WFJ, which supports the aerosol analysis carried out in Section 3.1. These results are robust, indicating that for non-precipitating BL clouds the proposed calculation method captures cloud droplet formation at WOP and WFJ.

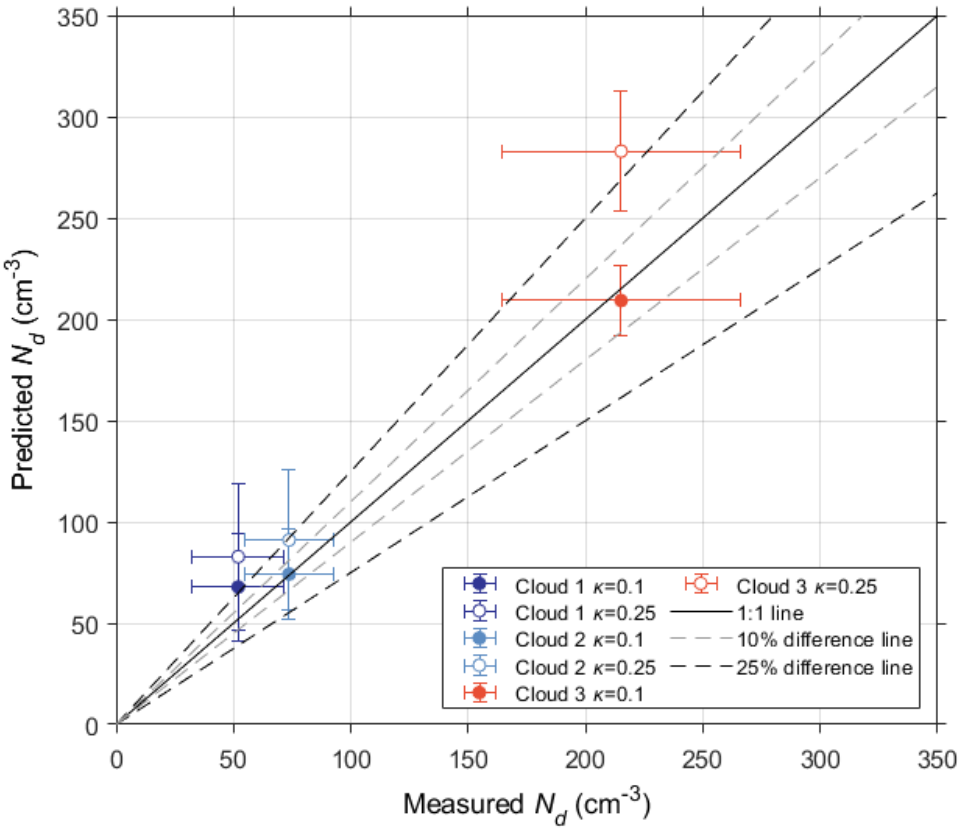

Figure 6. Comparison between average predicted N_d (cm^{-3}) with the droplet activation parameterization and N_d (cm^{-3}) observed during the three cloud events on the 7th (blue and cyan circles) and the 8th of March (orange circles) 2019. For all three cloud events droplet closure is performed assuming a κ parameter of 0.1 (filled circles) and 0.25 (empty circles). The error bars represent the standard deviation of N_d during each cloud event.

3.2.2 Droplet formation at WOP and WFJ

According to the methodology proposed in Section 2.3, using the in-situ measured N_{aer}, the estimated chemical composition and the observed updraft velocity range, we determine the N_d and S_{max} that would form over both measurement sites. At WOP, clouds are formed locally due to the local topography (Ramelli et al., 2020b, c), supporting the use of surface measured aerosol to estimate the potential N_d over this site. This is further supported by the good degree of droplet closure (Section 3.2.1). A similar closure study could not be repeated for WFJ owing to a lack of in-situ data, however the airmasses sampled (i.e. those given as input to the parameterization) are often in the FT, so they should contain the same aerosol as the one used to form the clouds. This does not apply under perturbed FT conditions, which are however accompanied by the presence of less hygroscopic particles over the mountain-top site and are less likely related to cloud formation (Section 3.1). Here we assume a κ of 0.25 to calculate the potential droplets for WFJ according to our CCN-derived hygroscopicity values (Table 2) and

given that S_{max} usually ranges between ∽0.1-0.3%. In estimating the potential droplets for WOP, we use a κ of 0.1 given that aerosol is likely strongly enriched in organics; the good degree of closure that this value supports its selection (Section 3.2.1). Figure 7 depicts the potential N_d and the corresponding S_{max} timeseries calculated at ambient conditions for WOP (orange dots) and WFJ (blue dots) using cloud updraft velocities that are indicative of the observed σ_w range (Section 3.4), namely 0.1, 0.3, 0.6 and 0.9 ms^{-1}. The same behavior is seen for all four σ_w values selected while, as expected, larger values of N_d and S_{max} are achieved at higher σ_w. During the first days of the period of interest, the calculated N_d at WOP (Fig. 7a, c, e, g) is up to 10 times larger than at WFJ, despite the lower κ values characterizing its aerosol population. WFJ tends to have lower N_d due to the lower N_{aer} recorded. It is also important to highlight the anticorrelation between S_{max} and N_d values arising from the nonlinear response of droplet number and maximum cloud parcel supersaturation to fluctuations in the available aerosol/CCN concentrations (Reutter et al., 2009; Bougiatioti et al., 2016; Kalkavouras et al., 2019). Higher N_{aer} elevates N_d values. The available condensable water is then shared among more growing droplets, depleting the supersaturation. Even more interesting is the fact that until February 28 the calculated N_d timeseries at WOP show a pronounced diurnal cycle, similar to the total N_{aer} timeseries (Section 3.1). Lower N_d values are visible during nighttime due to the limited turbulence. Droplet concentrations at WFJ do not follow a diurnal pattern in contrast to the aerosol data (Fig. 1a). However, the activation fraction (i.e. N_d/N_{aer}) at WFJ displays a clear diurnal variability until the end of February (supplement Fig. S5).

Through comparison with the MeteoSwiss precipitation measurements at WFJ (Fig. 4), it should be emphasized again that during the second sub-period of interest the occurrence of precipitation is followed by a depression in N_d (Fig. 7a, c, e, g) and a concurrent increase in S_{max} reaching up to ∽1% (Fig. 7b, d, f, h). Especially at WFJ, N_d drops almost to zero on the 1st, the 4th and the 7th of March, when precipitation is most intense (blue-shaded areas in Fig. 2 and 7). These trends are related to the washout of hygroscopic material observed at WFJ (Fig. 2) leading to the extremely low CCN concentrations (∽10 cm^{-3}) measured during these three days. During the first two intense precipitation events, the N_{aer} is relatively high, compared to the third event, with concentrations reaching up to ∽300 cm^{-3} at both stations. The small activation fraction (supplement Fig. S5) combined with the high S_{max} values indicates once more that small particles that activate into cloud droplets only above 0.3 to 0.5% of supersaturation are present at both stations. However, this behavior is not seen on March 7 at WFJ.

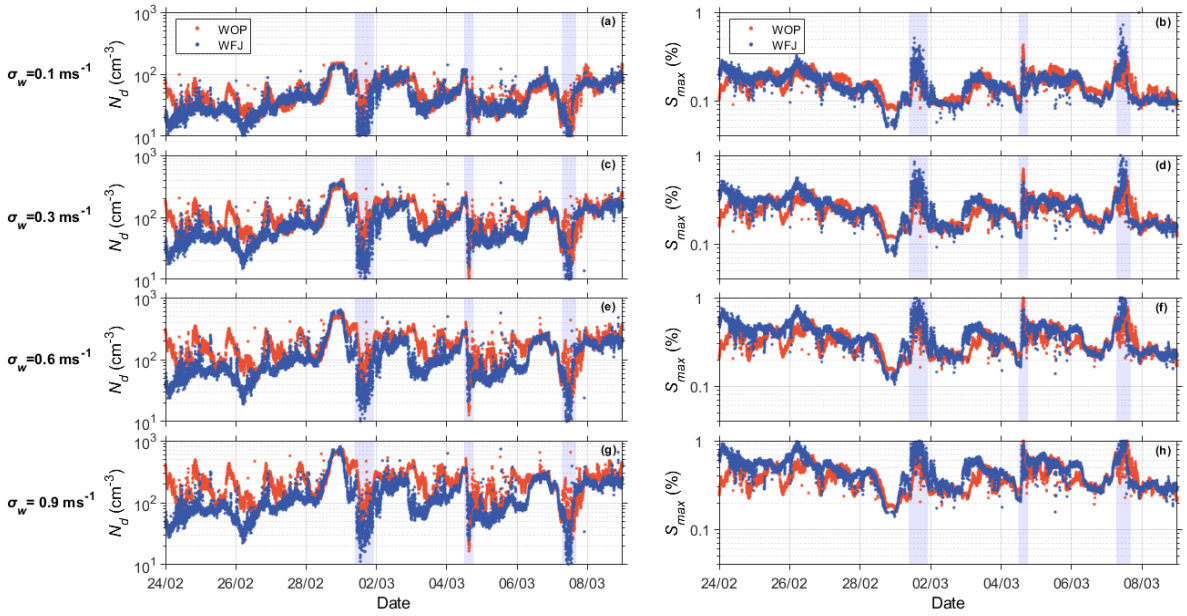

Figure 7. Calculated timeseries of N_d (cm^{-3}) (left panels) and S_{max} (%) (right panels), for updraft velocities of σ_w = 0.1 ms^{-1} in a and b, 0.3 ms^{-1} in c and d, 0.6 ms^{-1} in e and f, and 0.9 ms^{-1} in g and h, during the period of interest at WOP (orange dots) and WFJ (blue dots). The blue-shaded areas represent the intense precipitating periods as shown in Figure 2.

3.2.3 Droplet behavior under velocity-limited conditions

Combining the potential N_d and the corresponding S_{max} with the N_{aer} data yields important information on whether clouds are sensitive to vertical velocity or aerosol changes. Cloud studies (e.g., Jensen and Charlson, 1984; Twomey, 1993; Ghan et al., 1998, Nenes et al., 2001 and Reutter et al., 2009) have long recognized the role of water vapor competition on droplet formation, while the success of mechanistic parameterizations for climate models relies on the ability to capture this effect accurately (e.g., Ghan et al., 2011; Morales and Nenes, 2014). Twomey (1993) discusses this conceptually and states that competition may be fierce enough to reduce N_d with increasing N_{aer}, which was later demonstrated by Ghan et al. (1998) to occur for mixtures of sulfate aerosol and sea spray. Reutter et al. (2009) did not focus on such extreme conditions of water vapor competition, but rather situations that are consistent with dominance of anthropogenic pollution in clouds. Indeed, for high N_{aer}, droplets in clouds become insensitive to aerosol perturbations, giving rise to the so-called "velocity limited cloud formation". Figure 8 displays this, presenting the response of the calculated N_d to changes in N_{aer} for a representative range of updraft velocities prevailing over WOP (top panels) and WFJ (bottom panels). The data are colored by the respective S_{max} achieved in cloudy updrafts. For

low σ_w values (Fig. 8a, d) we can identify that above an N_{aer} of ∽300 cm^{-3}, the N_d at both stations reaches a plateau, where it becomes insensitive to further aerosol changes. At WFJ, the same behavior is seen for intermediate σ_w values and N_{aer} ≳1000 cm^{-3} (Fig. 8f). Kacarab et al. (2020) and Bougiatioti et al. (2020) examined a wide range of ambient size distributions and proposed that clouds became velocity-limited when S_{max} dropped below 0.1%. This reflects the increasingly fierce competition for water vapor during droplet formation, which allows only a few particles to activate into cloud droplets.

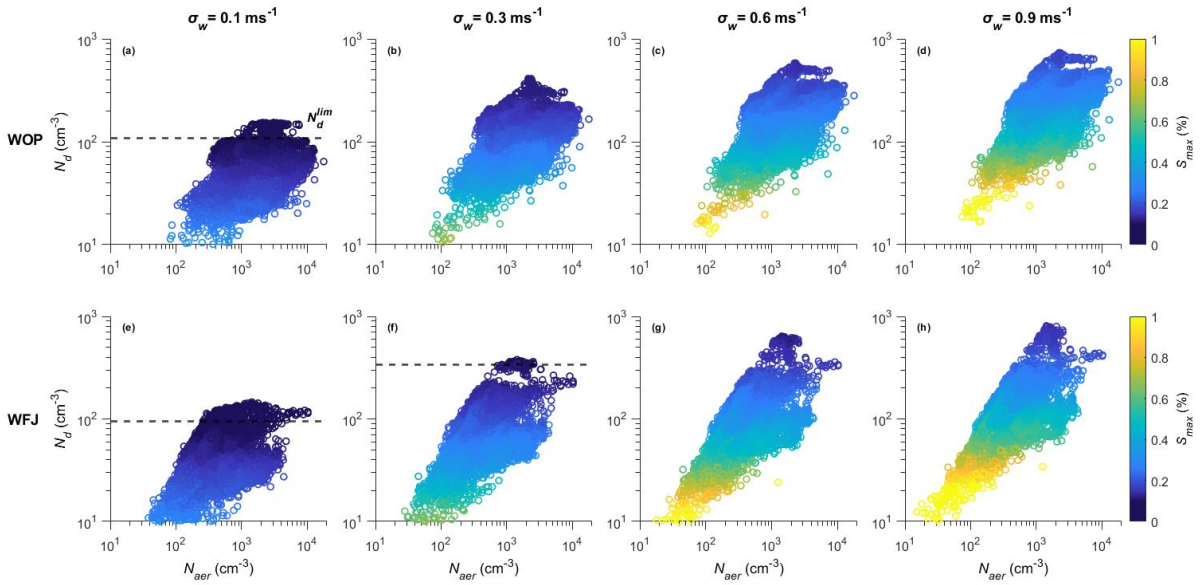

Figure 8. In-situ N_d (cm^{-3}) vs. N_{aer} (cm^{-3}), for updraft velocities of σ_w = 0.1 ms^{-1} in a and e, 0.3 ms^{-1} in b and f, 0.6 ms^{-1} in c and g and 0.9 ms^{-1} in d and h, during the period of interest at WOP (top panels) and WFJ (bottom panels). Data are colored by S_{max} (%).

Building upon these findings, we used the predicted S_{max} as an indicator for aerosol- or velocity-limited conditions prevailing over the Alps. The horizontal dashed lines plotted on Figure 8 (a), (e) and (f) illustrate a plateau, where S_{max} < 0.1% and the modulation of the N_d is driven mostly by the cloud dynamics, hence the updraft velocity variability, rather than aerosol variations. This plateau is termed limiting droplet number (N_d^{lim}), following Kacarab et al. (2020), and is essentially the maximum N_d that can be formed under these vertical velocity conditions. The vertical-velocity regime is therefore strictly defined, whenever S_{max} drops below 0.1% and N_d approaches N_d^{lim}. Conversely, when S_{max} in clouds exceeds 0.1%, droplet formation in the BL of both measurement sites is in the aerosol-limited regime, as the S_{max} is high enough for clouds to be responsive to aerosol changes.

An alternative way of examining the N_d^{lim} response to changes in σ_w is shown in Figure 9. It should be noted that the N_d^{lim} values shown on this figure are determined by calculating the averaged N_d achieved whenever S_{max} < 0.1 % for each examined σ_w value. At WOP, droplet formation is in the velocity-limited regime only for low σ_w values, namely 0.1 and 0.2 ms^{-1}, when the activated particles have more time to deplete the gas phase, and the S_{max} reached is that required to activate only the largest particles. At WFJ the prevailing dynamics create velocity-limited conditions even for more turbulent boundary layers when σ_w reaches up to 0.5 ms^{-1}. N_d^{lim} (cm^{-3}) is linearly correlated with σ_w (ms^{-1}) which can be described as $N_d^{lim} = 1137.9\,\sigma_w - 17.1$ (Fig. 9). As a result, doubling σ_w from 0.1 to 0.2 ms^{-1} increases N_d^{lim} by ∽60% for both sites, while transitioning from 0.2 to 0.4 ms^{-1} further increases N_d^{lim} by ∽45%, and finally an additional ∽20% increase in N_d^{lim} occurs for WFJ for the 0.4-0.5 ms^{-1} velocity range. Remarkable agreement is seen for corresponding trends between N_d^{lim} and σ_w calculated for marine Stratocumulus clouds formed under extensive BB aerosol plumes over the Southeast Atlantic (SEA) Ocean (Kacarab et al., 2020), along with BL clouds formed in the Southeast United States (SEUS) (Bougiatioti et al., 2020). Both studies have followed the same probabilistic approach for computing N_d as the one followed here. This realization is important as it implies that for regions where velocity-limited conditions are expected (i.e. under particularly high particle loads), $N_d \backsim N_d^{lim}$ and the N_d^{lim}-σ_w relationship can be used to diagnose σ_w from retrievals of droplet number for virtually any type of BL cloud, using a number of established methods (e.g. Snider et al., 2017; Grosvenor et al., 2018).

3.2.4 σ_w and observed N_d determine if droplet formation is aerosol- or velocity-limited

Observations of N_d when compared against N_d^{lim} can potentially be used to deduce if droplet formation is velocity- or aerosol-limited. This is important because it indicates whether aerosol fluctuations are expected to result in substantial N_d responses in clouds. The strong correlation between σ_w and N_d^{lim} enables this comparison. From the σ_w timeseries together with the linear N_d^{lim}-σ_w relationship (Section 3.2.3; Fig. 9) we obtain estimates of N_d^{lim} for both measurement stations (black dashed line in Fig. 10a, b) and the ratio N_d/N_d^{lim} (magenta dotted lines in Fig. 10a, b). The N_d timeseries calculated for WOP tend to be approximately one third of N_d^{lim} for most of the observational period (colored circles in Fig. 10a, b), while for WFJ the same ratio is even lower ∽1/4. Focusing on the relatively short periods when S_{max} values drop below 0.1%, we estimate that droplet formation over both measurement sites enters a velocity-limited

700 regime when the ratio N_d/N_d^{lim} exceeds a critical value of 0.65, with the most prevalent value
701 being at ∽0.9 (supplement Fig. S6).

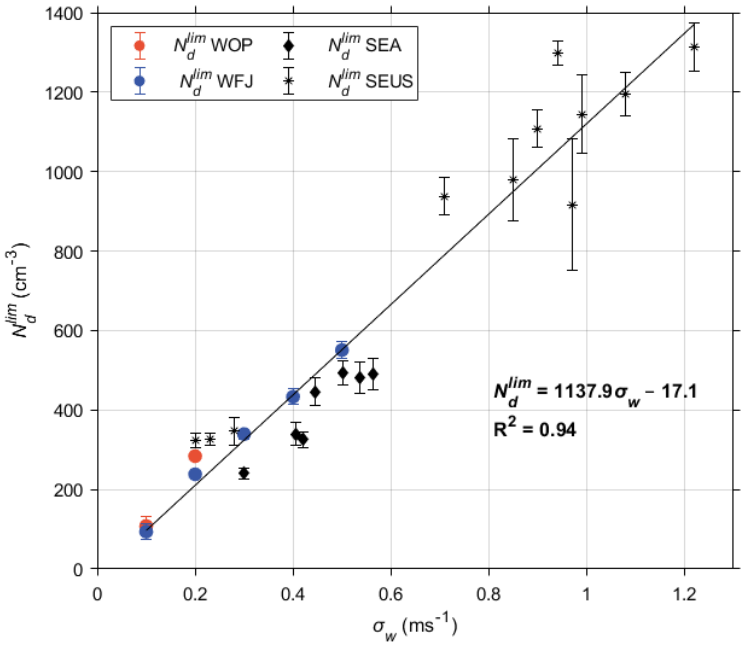

702

703 **Figure 9.** Limiting droplet number (cm^{-3}) against the standard deviation of updraft velocities
704 (ms^{-1}), calculated when vertical-velocity conditions are met over WOP (orange circles) and
705 WFJ (blue circles) sites throughout the period of interest. Superimposed are the corresponding
706 values calculated for clouds forming over the SEA Ocean (rhombuses) and over the SEUS
707 (asterisks).

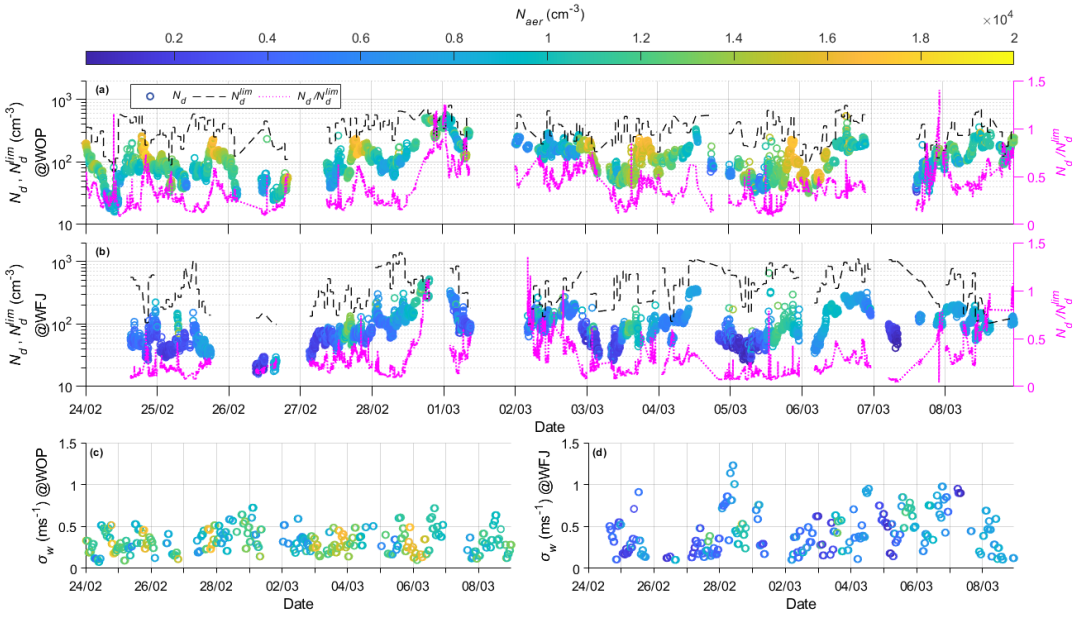

708

709 **Figure 10.** Timeseries of potential N_d (cm^{-3}) (circles colored by N_{aer}) along with N_d^{lim} (cm^{-3})
710 (black dashed line) and the ratio between those two (i.e. N_d/N_d^{lim}) (magenta dotted line),
711 together with the timeseries of the calculated standard deviation of updraft velocities (ms^{-1})
712 (circles colored by N_{aer}), as estimated for WOP (a, c) and WFJ (b, d).

Throughout the period of interest velocity-limited conditions are met at WOP (WFJ) with a frequency of ∽0.5% (∽2.5%) of the total time, reflecting again the sensitivity of droplet formation to aerosol fluctuations. During nighttime however, when lower σ_w values (∽0.1 ms^{-1}) are recorded at WOP (Fig. 10c), we can observe some short periods characterized by intermediate to high N_{aer} (> 1000 cm^{-3}) when the ratio N_d/N_d^{lim} exceeds ∽0.65, indicating that droplet variability is driven by updraft velocity. The σ_w values calculated at WFJ do not display a clear temporal pattern (Fig. 10d) but are generally higher than those recorded at the valley site. This is expected considering the steepness of the topography than can cause updraft velocities to be higher, especially for air-masses approaching the site from the north-easterly directions. Over the high mountain-top site cloud formation is in the velocity-limited regime (i.e. N_d/N_d^{lim} > 0.65) under high N_{aer} (∽1500 cm^{-3}) and higher σ_w conditions (∽0.8 ms^{-1}). These conditions can be created when polluted air-masses from the valley site are vertically transported to WFJ.

4. Summary and conclusions

The current study focuses on the aerosol-CCN-cloud droplet interplay in Alpine clouds sampled during the RACLETS field campaign over a two-week period of measurements conducted in the valley (WOP), and at the mountain-top station (WFJ). Our main objective was to investigate the drivers of droplet formation in MPCs formed in the region and understand in which situations N_d is sensitive to aerosol perturbations.

Overall, lower N_{aer} was systematically recorded at WFJ, indicating that the site is influenced by FT conditions. Deviations from this behavior are observed during fair weather conditions, when injections from the BL of lower altitudes can cause up to an order of magnitude elevation in the N_{aer} measured at WFJ. Combining the particle size distribution and CCN number concentration measured at WFJ, the average hygroscopicity parameter κ is about 0.25, consistent with expectations for continental aerosol. The size-dependent κ reveals that accumulation mode particles are more hygroscopic than the smaller ones, which we attribute to an enrichment in organic material associated with primary emissions in the valley. The hygroscopicity of the particles at WFJ exhibit variations until February 28, which could reflect BL injections from the valley. Precipitation events occurring between 1 and 8 March, efficiently decrease N_{aer}, sometimes leaving some less hygroscopic particles.

Wind lidar products collected at WOP constrain the PDF of updraft velocities, which combined with observed size distributions and hygroscopicity can be used to calculate the N_d in clouds. We show predictions to agree within 25% with the limited observations of N_d available. While this degree of closure has been achieved in past studies for liquid-phase clouds, it has not been done at temperatures below freezing and with clouds containing ice – as done here.

Combining the potential N_d and the corresponding S_{max} with the aerosol size distribution data we sought to identify regimes where clouds formed are aerosol- or velocity-limited. We found that when sufficient aerosol is present to decrease S_{max} below 0.1%, Alpine clouds become velocity-limited, with the N_d reaching an upper limit, N_d^{lim}, that depends on σ_w. Velocity-limited conditions occur when N_d/N_d^{lim} is above 0.65. Based on this understanding, we deduce that droplet formation throughout the period of interest appears most of the time to be aerosol-limited. More specifically, at the valley site, WOP, clouds become sensitive to updraft velocity variations only during nighttime, when the BL turbulence is low. Conversely, velocity-limited conditions are encountered at WFJ, during periods characterized by elevated aerosol and CCN concentration levels (>10^3 cm^{-3}) and higher σ_w values ($\backsim$0.8 ms^{-1}). Although variations in vertical velocity have not always been found to be the strongest factor influencing the cloud microphysical characteristics, correct consideration of updraft velocity fluctuations is crucial to fully understand the drivers of droplet variability and the role of aerosol as a driver of N_d variability.

Interestingly, we find that the same linear relationship between N_d^{lim} and σ_w that describes the droplet formation during RACLETS holds for warm boundary layer clouds formed in the SE US (Bougiatioti et al., 2020) and in the SE Atlantic (Kacarab et al., 2019). This implies that the N_d^{lim}-σ_w relationship may be universal, given the wide range of cloud formation conditions it represents. If so, measurements (or remote sensing) of N_d and vertical velocity distribution alone may be used to determine if cloud droplet formation is susceptible to aerosol variations or solely driven by vertical velocity – without any additional aerosol information.

Approaching velocity-limited conditions also carries important implications for ice-formation processes in MPCs – as high N_d means that droplet size and the probability of riming becomes minimum. Indeed, Lance et al. (2011) saw that the concentration of large droplets exceeding 30 μm diameter – critical for rime splintering or droplet shattering to occur – drops considerably for polluted Arctic MPCs with LWC ~ 0.2 gm^{-3} and N_d ~ 300-400 cm^{-3}. Assuming

778 that these levels of N_d reflects N_d^{lim}, the corresponding σ_w is 0.3-0.35 ms^{-1} (Fig. 9), which is
779 characteristic for Arctic stratus. The same phenomenon can also occur in the Alpine clouds
780 studied here, given that velocity-limited conditions (N_d/N_d^{lim}>0.65) occurs especially during
781 nighttime (Fig. 10). Therefore, observations of N_d and vertical velocity distribution (i.e., N_d^{lim})
782 may possibly be used to determine if SIP from riming and droplet shattering is impeded, and
783 if occurring frequently enough may help explain the existence of persistent MPCs.
784
785 **Data Availability:** The data used in this study can be downloaded from the EnviDat data portal
786 at https://www.envidat.ch/group/about/raclets-field-campaign. The meteorological
787 measurements are provided by the Swiss Federal Office of Meteorology and Climatology
788 MeteoSwiss at https://gate.meteoswiss.ch/idaweb/login.do. The Gaussian fits used for
789 determining σ_w and the droplet parameterization used for the calculations in the study are
790 available from athanasios.nenes@epfl.ch upon request.
791
792 **Author Contributions:** PG and AN designed and initiated the study with methodology and
793 software developed by AN. The analysis was carried out by PG and AN, with input from ABo,
794 JW, CM, ZAK, JH, MH, ABe, UL. CCN instrumentation was setup by ABo, aerosol
795 instrumentation and inlet setup were done by JW, CM and ZAK, cloud data by FR, JH, lidar
796 data by MH. Instrument maintenance during the field campaign was carried out by JW and
797 CM. Data curation was provided by PG, AN, JW, CM, FR. The original manuscript was written
798 by PG and AN with input from all authors. All authors reviewed and commented on the
799 manuscript.
800
801 **Funding:** This study was supported by the European Research Council, CoG-2016 project
802 PyroTRACH (726165) funded by H2020-EU.1.1. – Excellent Science, and from the European
803 Union Horizon 2020 project FORCeS under grant agreement No 821205. JW, FR, ZAK, JH,
804 UL acknowledge funding from the Swiss National Science Foundation (SNSF) grant number
805 200021_175824. CM acknowledges funding from the SNSF grant number 200021_169620.
806
807 **Conflicts of Interest:** The authors declare no conflict of interest.

References

Andreae, M. O. and Rosenfeld, D.: Aerosol-cloud-precipitation interactions. Part 1. The nature and sources of cloud-active aerosols, Earth-Science Rev., 89, 13–41, doi:10.1016/j.earscirev.2008.03.001, 2008.

Baltensperger, U., Gäggeler, H. W., Jost, D. T., Lugauer, M., Schwikowski, M., Weingartner, E. and Seibert, P.: Aerosol climatology at the high-alpine site Jungfraujoch, Switzerland, J. Geophys. Res., 102, 1997.

Barahona, D., West, R. E. L., Stier, P., Romakkaniemi, S., Kokkola, H. and Nenes, A.: Comprehensively accounting for the effect of giant CCN in cloud activation parameterizations, Atmos. Chem. Phys., 10, 2467–2473, doi:10.5194/acp-10-2467-2010, 2010.

Barahona, D., Molod, A., Bacmeister, J., Nenes, A., Gettelman, A., Morrison, H., Phillips, V., and Eichmann, A.: Development of two-moment cloud microphysics for liquid and ice within the NASA Goddard Earth Observing System Model (GEOS-5), Geosci. Model Dev., 7, 1733–1766, doi:10.5194/gmd-7-1733-2014, 2014.

Beck, A., Henneberger, J., Schöpfer, S., Fugal, J. and Lohmann, U.: HoloGondel: In situ cloud observations on a cable car in the Swiss Alps using a holographic imager, Atmos. Meas. Tech., 10, 459–476, doi:10.5194/amt-10-459-2017, 2017.

Bergeron, T.: On the physics of clouds and precipitation, Report, Int. Union Geod. Geophys., doi:10.1038/174957a0, 1935.

Borys, R. D., Lowenthal, D. H., Cohn, S. A. and Brown, W. O. J.: Mountaintop and radar measurements of anthropogenic aerosol effects on snow growth and snowfall rate, Geophys. Res. Lett., 30, doi:10.1029/2002gl016855, 2003.

Bougiatioti, A., Bezantakos, S., Stavroulas, I., Kalivitis, N., Kokkalis, P., Biskos, G., Mihalopoulos, N., Papayannis, A. and Nenes, A.: Biomass-burning impact on CCN number, hygroscopicity and cloud formation during summertime in the eastern Mediterranean, Atmos. Chem. Phys., 16, 7389–7409, doi:10.5194/acp-16-7389-2016, 2016.

Bougiatioti, A., Nenes, A., Lin, J., Brock, C., de Gouw, J., Liao, J., Middlebrook, A. and Welti, A.: Drivers of cloud droplet number variability in the summertime Southeast United States, Atmos. Chem. Phys., 20, doi:10.5194/acp-20-12163-2020, 2020.

Chow, F. K., De Wekker, Stephan, F. J. and Snyder, B. J.: Mountain weather research and forecasting: recent progress and current challenges., Dordrecht: Springer, 2013. Internet resource.

Conant, W. C., VanReken, T. M., Rissman, T. A., Varutbangkul, V., Jonsson, H. H., Nenes, A., Jimenez, J. L., Delia, A. E., Bahreini, R., Roberts, G. C., Flagan, R. C., and Seinfeld, J. H.: Aerosol-cloud drop concentration closure in warm cumulus, J. Geophys. Res.-Atmos., 109, D13204, doi:10.1029/2003JD004324, 2004.

Dusek, U., Frank, G. P., Curtius, J., Drewnick, F., Schneider, J., Krten, A., Rose, D., Andreae, M. O., Borrmann, S. and Pöschl, U.: Enhanced organic mass fraction and decreased hygroscopicity of cloud condensation nuclei (CCN) during new particle formation events, Geophys. Res. Lett., 37, L03804, doi:10.1029/2009GL040930, 2010.

Fanourgakis, G. S., Kanakidou, M., Nenes, A., Bauer, S. E., Bergman, T., Carslaw, K. S., Grini, A., Hamilton, D. S., Johnson, J. S., Karydis, V. A., Kirkevåg, A., Kodros, J. K., Lohmann, U., Luo, G., Makkonen, R., Matsui, H., Neubauer, D., Pierce, J. R., Schmale, J., Stier, P., Tsigaridis, K., van Noije, T., Wang, H., Watson-Parris, D., Westervelt, D. M., Yang, Y., Yoshioka, M., Daskalakis, N., Decesari, S., Gysel Beer, M., Kalivitis, N., Liu, X., Mahowald, N. M., Myriokefalitakis, S., Schrödner, R., Sfakianaki, M., Tsimpidi, A. P., Wu, M. and Yu, F.: Evaluation of global simulations of aerosol particle number and cloud condensation nuclei, and implications for cloud droplet formation, Atmos. Chem. Phys. Discuss., 19, 8591–8617, doi:10.5194/acp-19-8591-2019, 2019.

Farrington, R. J., Connolly, P. J., Lloyd, G., Bower, K. N., Flynn, M. J., Gallagher, M. W., Field, P. R., Dearden, C. and Choularton, T. W.: Comparing model and measured ice crystal concentrations in orographic clouds during the INUPIAQ campaign, Atmos. Chem. Phys., 16, 4945–4966, doi:10.5194/acp-16-4945-2016, 2016.

Field, P. R., Lawson, R. P., Brown, P. R. A., Lloyd, G., Westbrook, C., Moisseev, D., Miltenberger, A., Nenes, A., Blyth, A., Choularton, T., Connolly, P., Buehl, J., Crosier, J., Cui, Z., Dearden, C., DeMott, P., Flossmann, A., Heymsfield, A., Huang, Y., Kalesse, H., Kanji, Z. A., Korolev, A., Kirchgaessner, A., Lasher-Trapp, S., Leisner, T., McFarquhar, G., Phillips, V., Stith, J. and Sullivan, S.: Chapter 7. Secondary Ice Production - current state of the science and recommendations for the future, Meteorol. Monogr., doi:10.1175/amsmonographs-d-16-0014.1, 2017.

Findeisen, W.: Die kolloidmeteorologischen vorgänge bei der niederschlagsbildung, Meteorol. Zeitschrift, 55, 121–133, 1938.

Fountoukis, C. and Nenes, A.: Continued development of a cloud droplet formation parameterization for global climate models, J. Geophys. Res., 110, D1121, doi:10.1029/2004JD005591, 2005.

Fountoukis, C., Nenes, A., Meskhidze, N., Bahreini, R., Conant, W. C., Jonsson, H., Murphy,

S., Sorooshian, A., Varutbangkul, V., Brechtel, F., Flagan, R. C. and Seinfeld, J. H.: Aerosol-cloud drop concentration closure for clouds sampled during the International Consortium for Atmospheric Research on Transport and Transformation 2004 campaign, J. Geophys. Res., 112, doi:10.1029/2006JD007272, 2007.

Fugal, J. P., Schulz, T. J. and Shaw, R. A.: Practical methods for automated reconstruction and characterization of particles in digital in-line holograms, Meas. Sci. Technol., 20, doi:10.1088/0957-0233/20/7/075501, 2009.

Ghan, S., Guzman, G., and Abdul-Razzak, H.: Competition between sea salt and sulfate particles as cloud condensation nuclei, J. Atmos. Sci., 55, 3340–3347, 1998.

Ghan, S.J., Abdul-Razzak, H., Nenes, A., Ming, Y., Liu, X., Ovchinnikov, M., Shipway, B., Meskhidze, N., Xu, J. and Shi, X.: Droplet Nucleation: Physically-based Parameterization and Comparative Evaluation, J. Adv. Model. Earth Syst., 3, doi:10.1029/2011MS000074, 2011.

Griesche, H. J., Seifert, P., Ansmann, A., Baars, H., Barrientos Velasco, C., Bühl, J., Engelmann, R., Radenz, M. and Zhenping, Y.: Application of the shipborne remote sensing supersite OCEANET for profiling of Arctic aerosols and clouds during Polarstern cruise PS106, Atmos. Meas. Tech. Discuss., 1–37, doi:10.5194/amt-2019-434, 2019.

Grosvenor, D. P., Sourdeval, O., Zuidema, P., Ackerman, A., Alexandrov, M. D., Bennartz, R., Boers, R., Cairns, B., Chiu, J. C., Christensen, M., Deneke, H., Diamond, M., Feingold, G., Fridlind, A., Hünerbein, A., Knist, C., Kollias, P., Marshak, A., McCoy, D., Merk, D., Painemal, D., Rausch, J., Rosenfeld, J., Russchenberg, H., Seifert, P., Sinclair, K., Stier, P., van Diedenhoven, B., Wendisch, M., Werner, F., Wood, R., Zhang, Z. and Quaas, J.: Remote sensing of droplet number concentration in warm clouds: A review of the current state of knowledge and perspectives. Reviews of Geophysics, 56, 409–453. doi:10.1029/2017RG000593, 2018.

Grubisic, V. and Billings, B. J.: Climatology of the Sierra Nevada mountain-wave events, Mon. Weather Rev., 136, 757–768, doi:10.1175/2007MWR1902.1, 2008.

Hammer, E., Bukowiecki, N., Gysel, M., Jurányi, Z., Hoyle, C. R., Vogt, R., Baltensperger, U. and Weingartner, E.: Investigation of the effective peak supersaturation for liquid-phase clouds at the high-alpine site Jungfraujoch , Switzerland (3580 m a.s.l.), Atmos. Chem. Phys., 14, 1123–1139, doi:10.5194/acp-14-1123- 2014, 2014.

Hammer, E., Bukowiecki, N., Luo, B. P., Lohmann, U., Marcolli, C., Weingartner, E., Baltensperger, U. and Hoyle, C. R.: Sensitivity estimations for cloud droplet formation in the vicinity of the high-alpine research station Jungfraujoch (3580 m a.s.l.), Atmos. Chem.

910 Phys., 15, 10309–10323, doi:10.5194/acp-15-10309-2015, 2015.
911 Henneberg, O., Henneberger, J. and Lohmann, U.: Formation and development of orographic
912 mixed-phase clouds, J. Atmos. Sci., 74, 3703–3724, doi:10.1175/JAS-D-16-0348.1, 2017.
913 Henneberger, J., Fugal, J. P., Stetzer, O. and Lohmann, U.: HOLIMO II: A digital holographic
914 instrument for ground-based in situ observations of microphysical properties of mixed-
915 phase clouds, Atmos. Meas. Tech., 6, 2975–2987, doi:10.5194/amt-6-2975-2013, 2013.
916 Herrmann, E., Weingartner, E., Henne, S., Vuilleumier, L., Bukowiecki, N., Steinbacher, M.,
917 Conen, F., Collaud Coen, M., Hammer, E., Jurányi, Z., Baltensperger, U. and Gysel, M.:
918 Analysis of long-term aerosol size distribution data from Jungfraujoch with emphasis on
919 free tropospheric conditions, cloud influence, and air mass transport, J. Geophys. Res.
920 Atmos., 120, 9459–9480, doi:10.1002/2015JD023660, 2015.
921 Hoyle, C. R., Webster, C. S., Rieder, H. E., Nenes, A., Hammer, E., Herrmann, E., Gysel, M.,
922 Bukowiecki, N., Weingartner, E., Steinbacher, M. and Baltensperger, U.: Chemical and
923 physical influences on aerosol activation in liquid clouds : a study based on observations
924 from the Jungfraujoch , Switzerland, Atmos. Chem. Phys., 16, 4043–4061,
925 doi:10.5194/acp-16-4043-2016, 2016.
926 IPCC: Climate Change 2013: The Physical Science Basis. Contribution of Working Group I to
927 the Fifth Assessment Report of the Intergovernmental Panel on Climate Change, edited
928 by: Stocker, T. F., Qin, D., Plattner, G.-K., Tignor, M., Allen, S. K., Boschung, Cambridge
929 Univ. Press. Cambridge, UK New York, NY, USA, 1535 pp.,
930 doi:10.1017/CBO9781107415324, 2013.
931 Jensen, J. B. and Charlson R. J.: On the efficiency of nucleation scavenging, Tellus, 36B, 367–
932 375, doi: 10.3402/tellusb.v36i5.14917, 1984.
933 Jurányi, Z., Gysel, M., Weingartner, E., Decarlo, P. F., Kammermann, L. and Baltensperger,
934 U.: Measured and modelled cloud condensation nuclei number concentration at the high
935 alpine site Jungfraujoch, Atmos. Chem. Phys., 10, 7891–7906, doi:10.5194/acp-10-7891-
936 2010, 2010.
937 Jurányi, Z., Gysel, M., Weingartner, E., Bukowiecki, N., Kammermann, L. and Baltensperger,
938 U.: A 17 month climatology of the cloud condensation nuclei number concentration at the
939 high alpine site Jungfraujoch, J. Geophys. Res., 116, D1020, doi:10.1029/2010JD015199,
940 2011.
941 Kacarab, M., Lee Thornhill, K., Dobracki, A., Howell, S. G., O'Brien, J. R., Freitag, S., Poellot,
942 M. R., Wood, R., Zuidema, P., Redemann, J. and Nenes, A.: Biomass burning aerosol as
943 a modulator of the droplet number in the southeast Atlantic region, Atmos. Chem. Phys.,

20, 3029–3040, doi:10.5194/acp-20-3029-2020, 2020.

Kalkavouras, P., Bougiatioti, A., Kalivitis, N., Stavroulas, I., Tombrou, M., Nenes, A. and Mihalopoulos, N.: Regional new particle formation as modulators of cloud condensation nuclei and cloud droplet number in the eastern Mediterranean, Atmos. Chem. Phys., 19, 6185–6203, doi:10.5194/acp-19-6185-2019, 2019.

Kammermann, L., Gysel, M., Weingartner, E. and Baltensperger, U.: 13-month climatology of the aerosol hygroscopicity at the free tropospheric site Jungfraujoch (3580 m a.s.l.), Atmos. Chem. Phys., 10, doi:10.5194/acp-10-10717-2010, 2010.

Kleissl, J., Honrath, R. E., Dziobak, M. P., Tanner, D., Val Martín, M., Owen, R. C. and Helmig, D.: Occurrence of upslope flows at the Pico mountaintop observatory: A case study of orographic flows on a small, volcanic island, J. Geophys. Res. Atmos., 112, D10S3, doi:10.1029/2006JD007565, 2007.

Korolev, A. and Isaac, G.: Phase transformation of mixed-phase clouds, Q. J. R. Meteorol. Soc., 129, 19–38, doi:10.1256/qj.01.203, 2003.

Lance, S., Shupe, M. D., Feingold, G., Brock, C. A., Cozic, J., Holloway, J. S., Moore, R. H., Nenes, A., Schwarz, J. P., Spackman, J. R., Froyd, K. D., Murphy, D. M., Brioude, J., Cooper, O. R., Stohl, A. and Burkhart, J. F.: Cloud condensation nuclei as a modulator of ice processes in Arctic mixed-phase clouds, Atmos. Chem. Phys., 11, 8003–8015, doi:10.5194/acp-11-8003-2011, 2011.

Lanz, V. A., Pŕevôt, A. S. H., Alfarra, M. R., Weimer, S., Mohr, C., Decarlo, P. F., Gianini, M. F. D., Hueglin, C., Schneider, J., Favez, O., D'Anna, B., George, C. and Baltensperger, U.: Characterization of aerosol chemical composition with aerosol mass spectrometry in Central Europe: An overview, Atmos. Chem. Phys., 10, 10453–10471, doi:10.5194/acp-10-10453-2010, 2010.

Lathem, T. L., Beyersdorf, A. J., Thornhill, K. L., Winstead, E. L., Cubison, M. J., Hecobian, A., Jimenez, J. L., Weber, R. J., Anderson, B. E. and Nenes, A.: Analysis of CCN activity of Arctic aerosol and Canadian biomass burning during summer 2008, Atmos. Chem. Phys., 13, 2735–2756, doi:10.5194/acp-13-2735-2013, 2013.

Lauber, A., Henneberger, J., Mignani, C., Ramelli, F., Pasquier, J., Wieder, J. and Lohmann, U.: Continuous secondary ice production initiated by updrafts through the melting layer in mountainous regions, 2020.

Lloyd, G., Choularton, T. W., Bower, K. N., Gallagher, M. W., Connolly, P. J., Flynn, M., Farrington, R., Crosier, J., Schlenczek, O., Fugal, J. and Henneberger, J.: The origins of ice crystals measured in mixed-phase clouds at the high-alpine site Jungfraujoch, Atmos.

978 Chem. Phys., 15, 12953–12969, doi:10.5194/acp-15-12953-2015, 2015.
979 Lohmann, U.: A glaciation indirect aerosol effect caused by soot aerosols, Geophys. Res. Lett.,
980 29(4), doi:10.1029/2001GL014357, 2002.
981 Lohmann, U. and Feichter, J.: Global indirect aerosol effects: a review, Atmos. Chem. Phys.,
982 5, 715–737, doi:10.5194/acp-5-715-2005, 2005.
983 Lohmann, U., Henneberger, J., Henneberg, O., Fugal, J. P., Bühl, J. and Kanji, Z. A.:
984 Persistence of orographic mixed-phase clouds, Geophys. Res. Lett., 43, 10512–10519,
985 doi:10.1002/2016GL071036, 2016.
986 Lohmann, U.: Anthropogenic Aerosol Influences on Mixed-Phase Clouds, Curr. Clim. Chang.
987 Reports, 3, 32–44, doi:10.1007/s40641-017-0059-9, 2017.
988 Meskhidze, N., Nenes, A., Conant, W. C. and Seinfeld, J. H.: Evaluation of a new cloud droplet
989 activation parameterization with in situ data from CRYSTAL-FACE and CSTRIPE, J.
990 Geophys. Res., 110, D1620, doi:10.1029/2004JD005703, 2005.
991 Mignani, C., Creamean, J. M., Zimmermann, L., Alewell, C., and Conen, F.: New type of
992 evidence for secondary ice formation at around −15 °C in mixed-phase clouds, Atmos.
993 Chem. Phys., 19, 877–886, doi:10.5194/acp-19-877-2019, 2019.
994 Mignani, C., Wieder, J., Sprenger, M. A., Kanji, Z. A., Henneberger, J., Alewell, C. and Conen,
995 F.: Towards parameterising atmospheric concentrations of ice-nucleating particles active
996 at moderate supercooling, Atmos. Chem. Phys., 21, 657–664, doi:10.5194/acp-21-657-
997 2021, 2021.
998 Moore, R. H., Bahreini, R., Brock, C. A., Froyd, K. D., Cozic, J., Holloway, J. S., Middlebrook,
999 A. M., Murphy, D. M. and Nenes, A.: Hygroscopicity and composition of Alaskan Arctic
1000 CCN during April 2008, Atmos. Chem. Phys., 11, 11807–11825, doi:10.5194/acp-11-
1001 11807-2011, 2011.
1002 Morales Betancourt, R. and Nenes, A.: Characteristic updrafts for computing distribution-
1003 averaged cloud droplet number and stratocumulus cloud properties, J. Geophys. Res., 115,
1004 D1822, doi:10.1029/2009JD013233, 2010.
1005 Morales Betancourt, R., Nenes, A., Jonsson, H., Flagan, R. C. and Seinfeld, J. H.: Evaluation
1006 of an entraining droplet activation parameterization using in situ cloud data, J. Geophys.
1007 Res., 116, D1520, doi:10.1029/2010JD015324, 2011.
1008 Morales Betancourt, R., and Nenes, A.: Aerosol Activation Parameterization: The population
1009 splitting concept revisited, Geosci.Mod.Dev., 7, 2345–2357, doi:10.5194/gmd-7-2345-
1010 2014, 2014.
1011 Mosimann, L, Weingartner, E. and Waldvogel A.: An analysis of accreted drop sizes and mass

on rimed snow crystals., J. Atmos. Sci., 51, 1548–1558, 1994.

Muhlbauer, A. and Lohmann, U.: Sensitivity studies of aerosol-cloud interactions in mixed-phase orographic precipitation, J. Atmos. Sci., 66, 2517–2538, doi:10.1175/2009JAS3001.1, 2009.

Nenes., A., Ghan, S., Abdul-Razzak, H., Chuang, P.Y., Seinfeld, J.H.: Kinetic Limitations on Cloud Droplet Formation and Impact on Cloud Albedo, Tellus, 53B, 133-149, 2001.

Nenes, A. and Seinfeld, J. H.: Parameterization of cloud droplet formation in global climate models, J. Geophys. Res., 108, 4415, doi:10.1029/2002jd002911, 2003.

Okamoto, S. and Tanimoto, H.: A review of atmospheric chemistry observations at mountain sites, Prog. Earth Planet. Sci., 3, 34, doi:10.1186/s40645-016-0109-2, 2016.

Petters, M. D. and Kreidenweis, S. M.: A single parameter representation of hygroscopic growth and cloud condensation nucleus activity, Atmos. Chem. Phys., 7, 1961–1971, doi:10.5194/acp-7-1961-2007, 2007.

Pringle, K. J., Tost, H., Pozzer, A., Pöschl, U. and Lelieveld, J.: Global distribution of the effective aerosol hygroscopicity parameter for CCN activation, Atmos. Chem. Phys., 10, 5241–5255, doi:10.5194/acp-10-5241-2010, 2010.

Pruppacher, H. R. and Klett, J. D.: Microphysics of Clouds and Precipitation, 2nd ed., 1997.

Ramelli, F., Beck, A., Henneberger, J. and Lohmann, U.: Using a holographic imager on a tethered balloon system for microphysical observations of boundary layer clouds, Atmos. Meas. Tech., 13, 925–939, doi:10.5194/amt-13-925-2020, 2020a.

Ramelli, F., Henneberger, J., David, R. O., Lauber, A., Pasquier, J. T., Wieder, J., Bühl, J., Seifert, P., Engelmann, R., Hervo, M. and Lohmann, U.: Influence of low-level blocking and turbulence on the microphysics of a mixed-phase cloud in an inner-Alpine valley, Atmos. Chem. Phys. Discuss., doi:10.5194/acp-2020-774, in review, 2020b.

Ramelli, F., Henneberger, J., David, R. O., Bühl, J., Radenz, M., Seifert, P., Wieder, J., Lauber, A., Pasquier, J. T., Engelmann, R., Mignani, C., Hervo, M. and Lohmann, U.: Microphysical investigation of the seeder and feeder region of an Alpine mixed-phase cloud, submitted manuscript, 2020c.

Reutter, P., Su, H., Trentmann, J., Simmel, M., Rose, D., Gunthe, S. S., Wernli, H., Andreae, M. O. and Pöschl, U.: Aerosol- and updraft-limited regimes of cloud droplet formation: Influence of particle number, size and hygroscopicity on the activation of cloud condensation nuclei (CCN), Atmos. Chem. Phys., 9, 7067–7080, doi:10.5194/acp-9-7067-2009, 2009.

Roberts, G. C. and Nenes, A.: A continuous-flow streamwise thermal-gradient CCN chamber

for atmospheric measurements, Aerosol Sci. Technol., 39(3), 206–221, doi:10.1080/027868290913988, 2005.

Roe, G. H.: Orographic Precipitation, Annu. Rev. Earth Planet. Sci., 33, 645–671, doi:10.1146/annurev.earth.33.092203.122541, 2005.

Rose, D., Gunthe, S. S., Mikhailov, E., Frank, G. P., Dusek, U., Andreae, M. O. and Pöschl, U.: Calibration and measurement uncertainties of a continuous-flow cloud condensation nuclei counter (DMT-CCNC): CCN activation of ammonium sulfate and sodium chloride aerosol particles in theory and experiment, Atmos. Chem. Phys., 8(5), 1153–1179, doi:10.5194/acp-8-1153-2008, 2008.

Rotunno, R. and Houze, R. A.: Lessons on orographic precipitation from the Mesoscale Alpine Programme, Q. J. R. Meteorol. Soc., 133, 811–830, doi:10.1002/qj.67, 2007.

Saleeby, S. M., Cotton, W. R., Lowenthal, D. and Messina, J.: Aerosol impacts on the microphysical growth processes of orographic snowfall, J. Appl. Meteorol. Climatol., 52, 834–852, doi:10.1175/JAMC-D-12-0193.1, 2013.

Seinfeld, J. H. and Pandis, S. N.: Atmospheric Chemistry and Physics: From Air Pollution to Climate Change, 2nd Edn., John Wiley, edited by: Hoboken, N. J., 2006.

Seinfeld, J. H., Bretherton, C., Carslaw, K. S., Coe, H., DeMott, P. J., Dunlea, E. J., Feingold, G., Ghan, S., Guenther, A. B., Kahn, R., Kraucunas, I., Kreidenweis, S. M., Molina, M. J., Nenes, A., Penner, J. E., Prather, K. A., Ramanathan, V., Ramaswamy, V., Rasch, P. J., Ravishankara, A. R., Rosenfeld, D., Stephens, G. and Wood, R.: Improving our fundamental understanding of the role of aerosol-cloud interactions in the climate system, Proc. Natl. Acad. Sci. U. S. A., 113, 5781–5790, doi:10.1073/pnas.1514043113, 2016.

Smith, R. B.: Progress on the theory of orographic precipitation, Spec. Pap. Geol. Soc. Am., 398, 1–16, doi:10.1130/2006.2398(01), 2006.

Snider, J. R., Leon, D. and Wang, Z.: Droplet concentration and spectral broadening in Southeast Pacific stratocumulus clouds, J. Atmos. Sci., 74(3), 719–749. doi:10.1175/JAS-D-16-0043.1, 2017.

Sotiropoulou, G., Sullivan, S., Savre, J., Lloyd, G., Lachlan-Cope, T., Ekman, A. M. L. and Nenes, A.: The impact of secondary ice production on Arctic stratocumulus, Atmos. Chem. Phys., 20, 1301–1316, doi:10.5194/acp-20-1301-2020, 2020.

Sotiropoulou, G., Vignon, É., Young, G., Morrison, H., O'Shea, S. J., Lachlan-Cope, T., Berne, A., and Nenes, A.: Secondary ice production in summer clouds over the Antarctic coast: an underappreciated process in atmospheric models, Atmos. Chem. Phys., 21, 755–771, https://doi.org/10.5194/acp-21-755-2021, 2021.

Sud, Y.C, Lee, D., Oreopoulos, L., Barahona, D., Nenes, A. and M.J. Suarez: Performance of McRAS-AC in the GEOS-5 AGCM: aerosol-cloud-microphysics, precipitation, cloud radiative effects, and circulation, Geosci. Model. Dev., 6, 57–79, doi:10.5194/gmd-6-57-2013, 2013.

Sullivan, S. C., Lee, D., Oreopoulos, L. and Nenesa, A.: Role of updraft velocity in temporal variability of global cloud hydrometeor number, Proc. Natl. Acad. Sci. U. S. A., 113, 5791–5796, doi:10.1073/pnas.1514039113, 2016.

Sullivan, S. C., Barthlott, C., Crosier, J., Zhukov, I., Nenes, A. and Hoose, C.: The effect of secondary ice production parameterization on the simulation of a cold frontal rainband, Atmos. Chem. Phys., 18, 16461–16480, doi:10.5194/acp-18-16461-2018, 2018.

Tokay, A., Wolff, D. B. and Petersen, W. A.: Evaluation of the new version of the laser-optical disdrometer, OTT parsivel, J. Atmos. Ocean. Technol., 31(6), 1276–1288, doi:10.1175/JTECH-D-13-00174.1, 2014.

Touloupas, G., Lauber, A., Henneberger, J., Beck, A. and Lucchi, A.: A convolutional neural network for classifying cloud particles recorded by imaging probes, Atmos. Meas. Tech., 13(5), 2219–2239, doi:10.5194/amt-13-2219-2020, 2020.

Tröstl, J., Herrmann, E., Frege, C., Bianchi, F., Molteni, U., Bukowiecki, N., Hoyle, C. R., Steinbacher, M., Weingartner, E., Dommen, J., Gysel, M. and Baltensperger, U.: Contribution of new particle formation to the total aerosol concentration at the high-altitude site Jungfraujoch (3580masl, Switzerland), J. Geophys. Res. Atmos., 121, 11692–11711, doi:10.1002/2015JD024637, 2016.

Twomey, S., Radiative properties of clouds, pp. 278 – 280, in Aerosol Effects on Climate, S.G. Jennings Editor, The University of Arizona Press, Tucson, 1993.

Vosper, S. B., Wells, H., Sinclair, J. A. and Sheridan, P. F.: A climatology of lee waves over the UK derived from model forecasts, Meteorol. Appl., 20, 466–481, doi:10.1002/met.1311, 2013.

Wang, J., Lee, Y. N., Daum, P. H., Jayne, J. and Alexander, M. L.: Effects of aerosol organics on cloud condensation nucleus (CCN) concentration and first indirect aerosol effect, Atmos. Chem. Phys., 8, 6325–6339, doi:10.5194/acp-8-6325-2008, 2008.

Wegener, A.: Thermodynamik der Atmosphäre, Ger. Barth,Leipzig, 331 pp., 1911.

Zubler, E. M., Lohmann, U., Lüthi, D., Schär, C. and Muhlbauer, A.: Statistical analysis of aerosol effects on simulated mixed-phase clouds and precipitation in the Alps, J. Atmos. Sci., 68, 1474–1492, doi:10.1175/2011JAS3632.1, 2011.